Analyzing Exoplanet Survey Methods Using Massive Datasets
Transit and Microlensing Light Curves

By

Savannah Renee Jacklin

Dissertation

Submitted to the Faculty of the

Graduate School of Vanderbilt University

in partial fulfillment of the requirements

for the degree of

DOCTOR OF PHILOSOPHY

in

Astrophysics

May 8^{th}, 2020

Nashville, Tennessee

Approved:

Professor Keivan G. Stassun

Dr. Geoffrey Bryden

Professor Kelly Holley-Bockelmann

Professor Andreas Berlind

Dr. Natalie Hinkel

This thesis is dedicated to all of the helpers. It takes a village to raise a child, and to help that child through their education. I am forever grateful to the village of helpers who have been there for me throughout my journey.

ACKNOWLEDGMENTS

There are so very many thank yous I have to make, because the path to my PhD has not been completed in a vacuum. Therefore, and without further ado, I would like to thank: Elle McKenna and Abigail Searfoss, for being there to do all of the girly stuff even in fields where we work mostly with men. Kyle Godbey and Adam Szewciw, for getting into all this graduate school at the same time as me and for keeping absurdism alive and well. Colleen McHugh for being my best friend since the first day of kindergarten and for always being my cheerleader. Alyssa Cullere whose everyday awesomeness makes me proud to be your oldest friend. Erin Dobbs for keeping me consistently laughing about our study abroad in Russia, the constant flow of dog photos, and for helping me navigated the strange new waters of working with the government. All of the folks at Swing Dance Nashville, thanks for introducing me to the hobby that was the only thing that kept me sane at times. Sarah Bogdal for making sure I always made time for art. All the people who made California part one worth it, especially Ari Brown, Lindsey Marinello, and Patrick Kage. Rebecca Larson and Aurora Kesseli, who are both incredible astronomers who are the first people that made California feel like home. Phil Pearson and Jean Truong for making California part three feel a hell of a lot better. Dax Feliz, for being a calming presence in the office and for being the supreme New Yorker in the State of Tennessee. Calen Henderson for being both a friend and a mentor, and for throwing the most absurd parties I've attended. Kyle Conroy, who got me into this mess in the first place, and for being a real role model since we met way back in 2011. You showed me that someone from Villanova could go to grad school somewhere as awesome as Vanderbilt; thanks for helping me follow in your footsteps. Mike Lund, without whose help I would absolutely not have made it this far. Thank you for the haunted houses, the conference shenanigans, and the many, many times you drove all the way across Nashville to take me out to Cracker Barrel when you knew I could afford neither the gas nor the meal. Kyle Hawkins, for being one of the kindest people I have ever met. He is the one person I have have literally jumped off a cliff with, and his compassion over the years has helped shape me into the person I am today. John Hood, for his

unrelenting positivity and contagious laughter and pranks. George Vejar, for being the chill work personality to my salty one. Karl Jaehnig, for being there for literally every little thing, and for being my best friend in Nashville. Eric Stevens, who drove across the country for me (literally to both coasts), and have supported me with nothing but love through the hardest time in my life. I am grateful every day that we went to that Courtney Barnett concert together, and that you're willing to take fifty photos of us together just so we can find one where I'm not making a dumb face. My mom Valerie Jacklin, who is the most badass woman and scientist I know. Thank you for your support over the past 9 years of college and grad school, and for always helping me through tight spots with a clear head and a universe of experience. My dad Peter Jacklin, for sparking and fostering my love of science and figuring out how things work. My brother Tyler Jacklin, who never hesitates to tell me just how much he hates space, but who I know has always been a quiet supporter of my work. Katie Strauch and Sara Jacklin, who are more like sisters than cousins, and who keep me grounded. My Grandma and Bear, Theodore and Margaret Fedun, for being my number one fans. Back when I was about eight years old, they bought me my first ever astronomy book. It was directly because of that book that I am writing this thesis today. My Nana and Grandpa, Mary and Harry Jacklin, who have both passed away but who I know would be proud of the choices I've made to make it this far. All of the Jacklins and Feduns for supporting me in their own ways. And finally, my cat Stache for doing cat things that make me happy.

TABLE OF CONTENTS

LIST OF TABLES

LIST OF FIGURES

Chapter 1

Introduction

1.1 A Brief History of the Light Curve

When you are asked to picture an astronomer, what is the first image that comes to mind? Often, this thought experiment conjures up a Einstein-esque old man in a white lab coat squinting into the eyepiece of a comically proportioned telescope. Maybe he is holding a clipboard filled with graph paper, marked here and there with a scribble of numbers, a few exclamation points, and a squiggly looking line plot charted to go off the page altogether. If this approximates your vision of the typical astronomer, you would not be alone. In fact, a quick Google search of "cartoon astronomer" yields multitudinous images similar to the doodle in Figure 1.

Despite its popularity however, this image of a typical astronomer could not be further from the truth. In the year 2020, astronomers are rarely found looking into the eye piece of a telescope. Instead, we utilize charge-coupled devices (CCDs), which are complex digital cameras that collect and tally light on a pixel-by-pixel basis. Very little analysis is done on clipboards; most astronomers now analyze their observational and theoretical data using supercomputers. Today, astronomers come from a wide variety backgrounds, genders, ages, races and nationalities. Additionally, there are few remaining astronomers that study just one object at a time. Most of us now work and thrive in the nebulous world of "big data", processing information on scales that a basic laptop or desktop is no longer able to handle.

The rise of the CCD lead to a veritable boom in the in the field of transient astronomy. Astronomers are now able to observe large numbers of objects at once many times per night, generating enormous amounts of time-series data. The total light or flux of received from a source in the sky as a function of time yields a plot typically called a "light curve". The flux is also commonly referred to as the magnitude or brightness, and time is often measured in Julian Days (JDs). The number of data points in each light curve per unit of time is referred to as the light curve's cadence.

Figure 1.1: Typical cartoon of an astronomer (Image courtesy of shutterstock.com).

Modern astronomy has lead to a Pandora's box of high cadence light curves.

Thanks to advances in CCDs and other technologies, we are no longer restricted to studying the light that we can see with our eyes. Color filters and different telescope designs allow astronomers to study the entirety of the electromagnetic spectrum, from radio waves to gamma rays. Astronomers have even started to venture beyond the electromagnetic spectrum now that we have experienced the first detection of gravitational waves [1]. The overarching commonality between these different types of astronomical observations regardless of color, cadence, or flux is the fact that astronomers can use them to create a light curve. Light curves are tracers of variability in our seemingly static night sky, and scientists have always been interested in studying objects that change over time.

Identifying the particular patterns in a light curve can reveal a lot about the nature of the star system observed. Spikes in brightness over time can be attributed to a variety of variability scenarios, from solar flares to gravitational microlensing. The dimming of a star over time may mean that it is about to experience a supernova, or that it has an orbiting planet blocking some of its light. Changing light curves can be classified into two broad categories: periodic and non-periodic. Periodic signals are repetitive over time, creating patterns in light curves that astronomers use to understand a variety of different types of phenomena. Figure 1.2 shows an example of a periodic light curve of an RV Tau star that brightens and dims according to a regular pattern due to different modes of stellar pulsation.

Non periodic signals in light curves can also reveal a great deal about a system. One of the most famous recent examples of a non-periodic light curve comes from the so-called "Boyajian's Star". Otherwise known as KIC8462852, this *Kepler* star experienced erratic reductions in brightness during the time it was observed. The resultant light curve shown in Figure 1.3 lead to widespread public and scientific speculation on the variability's origin, with ideas ranging from alien mega-structures to disintegrating orbiting moons. Regardless of the periodicity or the extrema of changes in a light curve, any sign of variability of stars is a strong motivator for future study. This dissertation focuses on two very specific forms of observing and characterizing light curve

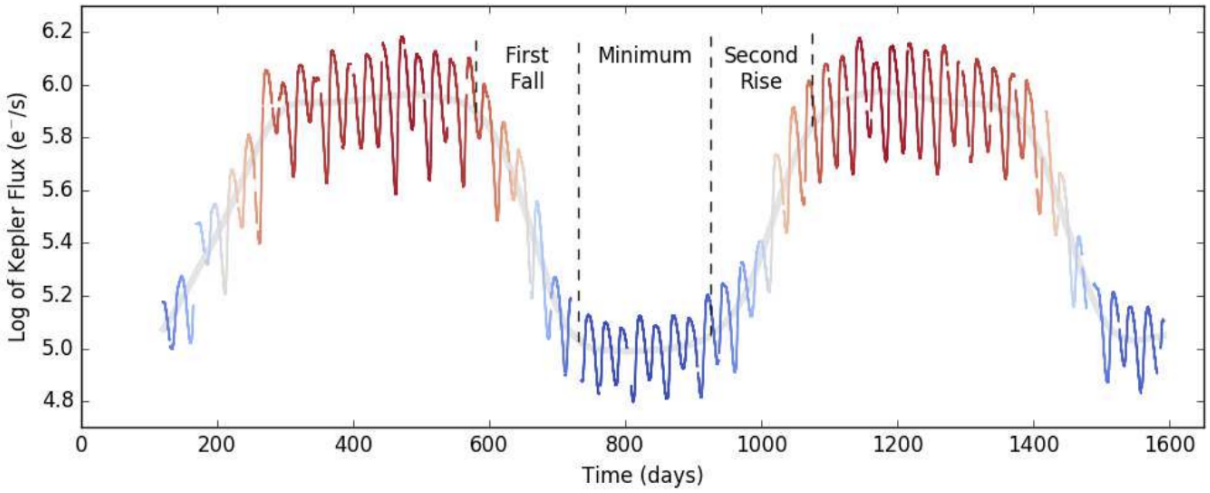

Figure 1.2: Example periodic light curve of the RV Tau star DF Cyg. This particular light curve shows two modes of variability; short and long term. The short period variability is evidenced in the sawtooth patterns in recorded flux, and the sinusoidal long period variability is marked by areas in red (bright) and blue (dim)[46].

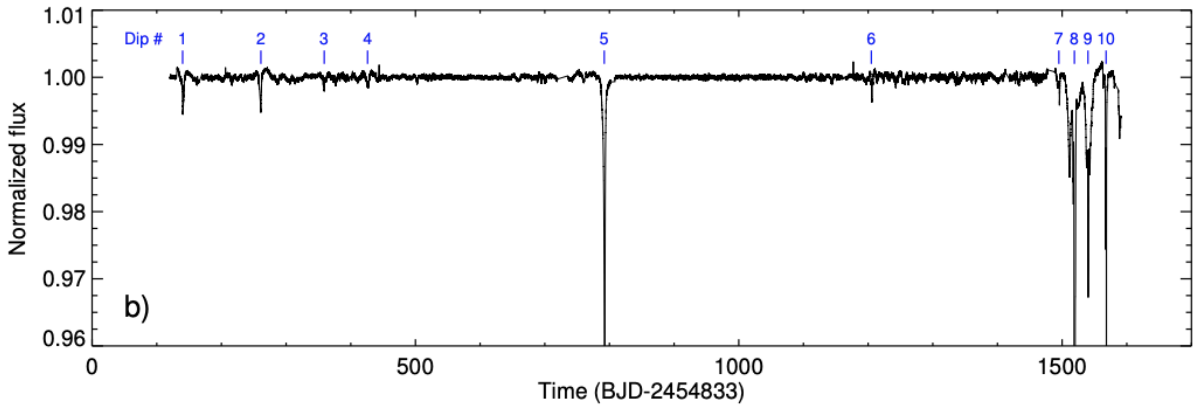

Figure 1.3: The light curve of Boyajian's star. These non-periodic dips in brightness ignited the imaginations of both the public and astronomers alike as many scrambled to try and determine the cause of the dimming. To date, no one solution has been determined [9].

variability: transits and gravitational microlensing. Both of these observational measures leverage the variability of light curves to discover new exoplanets, albeit very differently from one another. Each method is described in detail in the following sections.

1.2 Transits

The most prolific exoplanet detection method to-date is called the transit method. Employed by both space- and ground-based missions, the transit method looks for the periodic dimming of light from a host star as an orbiting planet eclipses its light from the perspective of an observer. Figure 1.4 shows a diagram of this process.

When a planet eclipses its host star, the dimming is periodic, achromatic, and has a characteristic "boxcar" shape. Astronomers can infer a great deal about the exoplanetary system by studying the shape of the transit dip in observed magnitude. The depth of reduction in flux is proportional to ratio of the planet radius to the star radius. That is, the larger the radius of the planet compared to the radius of its star, the more light it will block, and the greater the transit depth. The duration of the transit tells us about the period of the exoplanet. If the transit is very brief, then the planet is orbiting close to its star and has a short year. Conversely, if the duration of the transit is long, it can be inferred that the planet has a longer orbital period. The duration is also be related to the orientation angle of the transiting system with respect to the Earth. One must also note that exoplanet transits that appear to merely graze the edge of their host star will also have a shorter duration, but that grazing will have an effect other measurable aspects of the light curve.

There are a few notable examples of surveys specifically designed to detect transiting exoplanets. The *Kepler* space satellite (launched in 2011), for example, stared at one small patch of the sky for nearly four years at high cadence with the aim of finding a true Earth analog [8]. To date, *Kepler* has detected more candidate and confirmed exoplanets than any other survey. The more recent survey TESS (the Transiting Exoplanet Survey Satellite) attempts a different approach at exoplanet detection by approaching full sky coverage at the expense of unbroken cadence and magnitude depth [37]. Transiting exoplanets have also been detected by a variety of ground-based surveys such as the Kilodegree Extremely Little Telescope (KELT) [33] and MEARTH [29]. Chapters 2

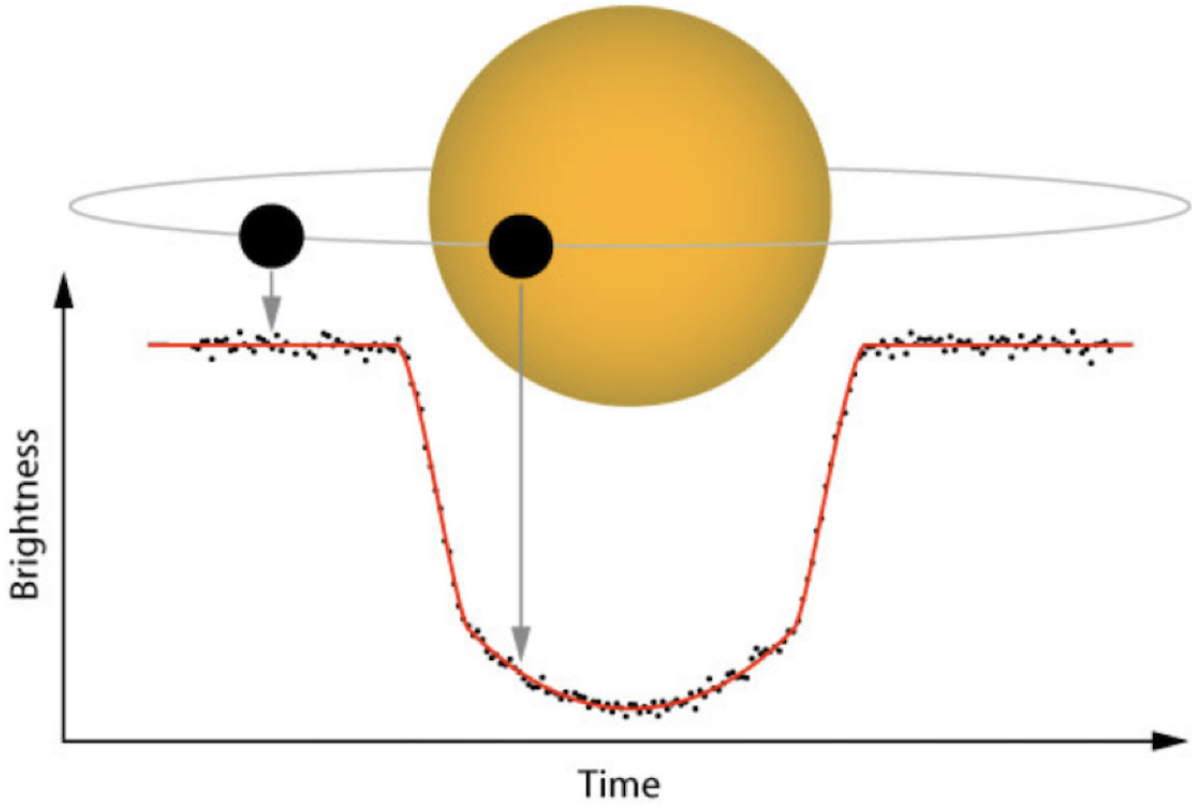

Figure 1.4: A diagram of the light curve of a transiting exoplanet as compared to a representation of the physical system.(Image courtesy of the TESS team)

and 3 will explore how the Vera Rubin Observatory (VRO), a ground-based telescope that was not designed with transiting exoplanets in mind, can still inform astronomers on exoplanetary statistics throughout our Galaxy and beyond using the transit method.

1.3 Microlensing

To appropriate a quote from the popular television series The Umbrella Academy, "A [transit] is trivial when compared with the unknowns of [gravitational microlensing]. One is like sliding along the ice, the other is akin to descending blindly into the depths of the freezing water and reappearing as an acorn" [7]. Transits are fairly straightforward; if you understand shadows, then you can understand the basic mechanics of transits. However, gravitational microlensing (microlensing for short) is a phenomenon that occurs when mass bends the very fabric of spacetime and alters the way light is perceived by an observer.

A gravitational microlensing system is comprised primarily of three components as shown in Figure 1.5. The first component is the observer, located either on Earth or as a satellite. The second component is a source star, which is a usually a red clump giant background star located in the Galactic Bulge approximately 8 kiloparsecs away. In-between the source and the observer is the lens system, which is usually a main sequence star located in either the Galactic Disk or Bulge which may be accompanied by a planet. In most cases, all of the light we see as an observer is coming from the source star as altered by the lens system. During a microlensing event, the gravitational potential well of the lens system acts like a magnifying glass in space, bending and subsequently magnifying the light from the source star as the three system components move in space, forming a nearly straight line. The bending angle of the lens system is called the Einstein ring radius θ_E and is defined as

$$\theta_E = \sqrt{\frac{4GM}{c^2}\left(\frac{1}{d_L} - \frac{1}{d_S}\right)}, \tag{1.1}$$

where G is the gravitational constant, M is the lens mass, c is the speed of light, d_L is the distance between the observer and the lens and d_S is the distance between the observer and the source. Each

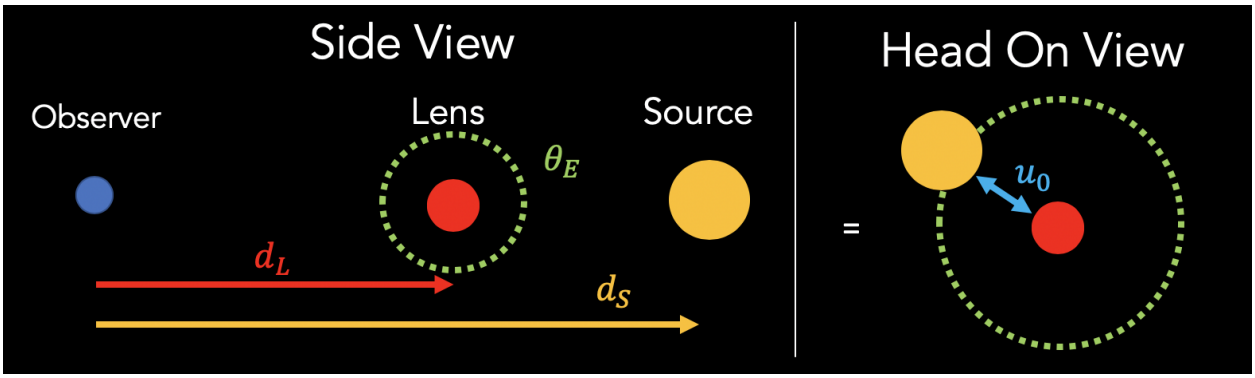

Figure 1.5: A diagram of the various components in a microlensing system. In some cases, the lens may have an orbiting planet.

of these variables will affect the shape of the resultant light curve, which takes on a characteristic bell shape of magnification over time. This magnification is usually highly significant, where the source star appear up to 1,000 times brighter than in their un-lensed state. A major driver of the magnitude change is the projected separation at closest approach u_0, which when combined with the time of closest approach t_0 and the duration of the event t_E yields the dimensionless quantity u

$$u(t) = \sqrt{u_0^2 + \left(\frac{t - t_0}{t_E}\right)^2}, \tag{1.2}$$

which is the angular separation of the lens and the source divided by θ_E. This can then be converted into a magnification A by:

$$A(u) = \frac{u^2 + u}{u\sqrt{u^2 + 4}}. \tag{1.3}$$

Several of these quantities can be effectively "read off" a microlensing light curve, as shown in Figure 1.6.

Microlensing events are relatively short-lived phenomena (of order 45 days on average) for main sequence lenses [17]. Since the event duration scales roughly with the lens mass, more exotic lenses such as white dwarfs and black holes extend this timescale. In order to capture enough of the light curve to generate a good parameter fit, microlensing surveys need to have good cadence coverage of the event, as well as the source star's baseline magnitude.

When Einstein first posited that gravitational microlensing would be a consequence of his theory of general relativity in 1936, he famously claimed that "there is no hope of observing this phenomenon directly" [16]. This is due to the issue that microlensing is an inherently rare phenomenon; there is less that an one-in-a-million chance per star per year of observing microlensing in the most crowded area of the night sky [17]. This number becomes even smaller when looking at less crowded fields such as the Galactic Disk. At the time Einstein made his claim, telescopic observations were still being made with photographic plates at very low cadence. The paucity of microlensing events combined with a lack of appropriate cadence, meant that microlensing was simply impossible to detect. However in the 21^{st} century, improved technologies such as the CCD and large scale, space-based, and worldwide telescope networks means that microlensing events

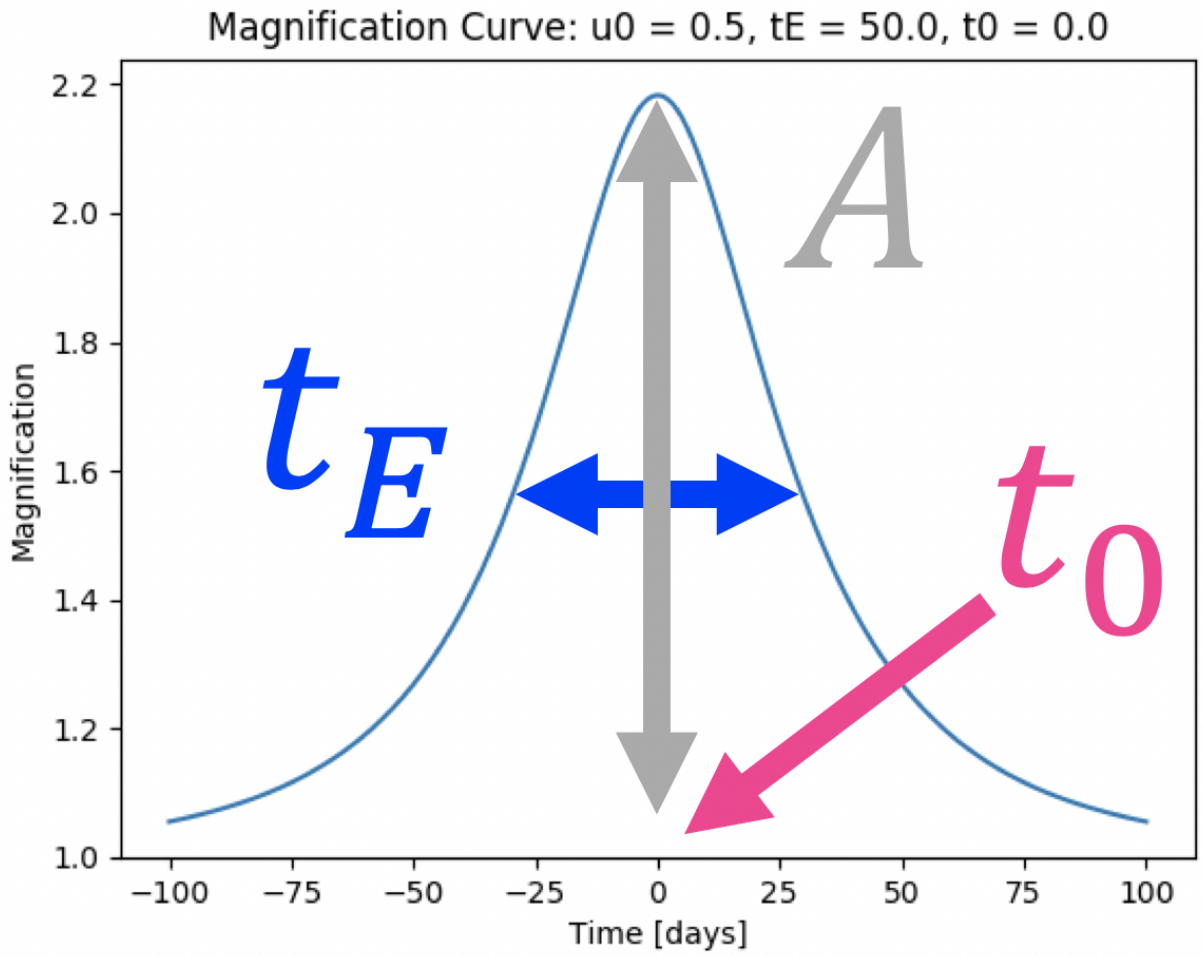

Figure 1.6: Given an single lens system (i.e. no planets), astronomers can approximate the magnification A, time of closest approach t_0, and event duration t_E simply by looking at the light curve.

are not only possible to detect, but are relatively common. The approximate event rate is still about $10^{-5}/star/year$, but astronomers are learning that this varies slightly by field, and better surveys mean that we can monitor many millions of stars at a time. Chapter 5 of this thesis explores one such microlensing survey with the United Kingdom Infrared Telescope (UKIRT). This survey's objective is to understand what kinds of microlensing events we can detect near the Galactic center, peering through obscuring dust using infrared wavelengths.

Chapter 2

Transiting Exoplanets with the Vera Rubin Observatory

2.1 The Vera Rubin Observatory

Starting in approximately 2021, the Vera Rubin Observatory (VRO) will begin operations from Cerro Pachón in Chile. As a wide-fast-deep survey, VRO is built to satisfy a wide variety of science goals over an unprecedented volume of space. Per Ivezic et al. [20] the mission has four primary science goals: understanding dark matter and dark energy, cataloging the solar system, Milky Way structure and formation, and the study of transient and variable objects (i.e. the changing sky). Using the visual and infrared filters *ugrizy*, VRO will observe a 20,000 square degree area of the southern sky in a deep-wide-fast synoptic survey to a depth of 24.5 mag per visit. Over ten years of observation, this amounts to about 30 terabytes of data taken by the telescope every night. The VRO survey will produce light curves for $\sim 10^9$ stars in the Milky Way and the Magellanic Clouds [25].

It was shown in Lund et al. [26] that VRO standard observations will be capable of detecting transiting planets in systems such as a $10R_\oplus$ planet orbiting a G-dwarf, a $4R_\oplus$ planet orbiting a K-dwarf, and a $2R_\oplus$ planet orbiting an M-dwarf. Following this proof of concept, Jacklin et al. [21] specifically aimed to quantify the recoverability of certain types of transiting planets as a function of planetary orbital period and planet radius.

To assess the question of planet detection with VRO, it is particularly important to account for the limitations and complexity of the two cadence strategies that VRO will employ over the course of its ten-year expected lifetime [20]. VRO will acquire pairs of 15-s exposures, hereafter treated and referred to as 34-s visits. Observations in most fields will have an average cadence of approximately 0.3 d^{-1}, but will usually involve multiple exposures in a single night separated by long gaps of many nights. Each standard field will have on the order of ~ 1000 distinct visits at "regular" cadence; see Fig 2.1 for the distribution of visits per field. Regular cadence observations will

consume about 90% of VRO's total observational schedule. In addition to the regular cadence, the VRO will observe a small number of fields (~ 10) at a much higher cadence, making about 10,000 visits over the course of the survey. This "deep-drilling" cadence will utilize the remaining 10% of VRO's observational schedule. The sheer size of the observational area, the very large number of target stars, and the large number of observations comprising the light curves suggest that VRO has the potential for the discovery of transiting exoplanets, particularly in stellar populations that are faint, distant, or otherwise less thoroughly probed by previous transit surveys.

Unlike missions such as *Kepler* [8] and TESS [36], or small, ground-based surveys such as KELT [33, 32], HATNet [2], or SuperWASP [35], VRO is not optimized for exoplanet detection. Although these cadences are not ideal for exoplanet detection, we showed in Lund et al. [26] and Jacklin et al. [21] that the sheer number of VRO targets ($\sim 10^9$) drastically increases the statistical likelihood of observing a planetary transit, particularly with respect to hot Jupiters and other short-period exoplanets.

One goal of this work is to consider the impact of these different cadences on the planet recoverability and detection in many interesting regions of parameter space. It is now known that there are a large variety of exoplanet system architectures, and therefore several astrophysical factors that ultimately influence the overall detectability of planets. These include host star size and rotational velocity; planet size, mass, and radius; planetary orbital period, eccentricity, and inclination; and host star photometric and spectroscopic variability. VRO's magnitude depth and sky coverage will include types of systems that are at present poorly explored. This includes planets orbiting nearby late-type stars and larger planets orbiting Sun-like stars at very large distances. We begin by examining the recoverability of a transiting planet's periodic photometric signal, focusing specifically on large planets with sizes of 5–14 $R_\oplus$ orbiting a 1 $M_\odot$ star at 7 kpc from the Earth. We then expand this analysis to include $0.6M_\odot$ and $0.25M_\odot$ stars with transiting hot Neptunes ($4 and 6R_\oplus$ and a hot Super Earth ($2R_\oplus$) respectively. It is also worth investigating how quickly VRO is likely to achieve various types of exoplanet discoveries over the course of its lifetime. In order to accomplish this goal, we use the VRO Operation Simulation (OpSim) of deep-drilling fields to predict

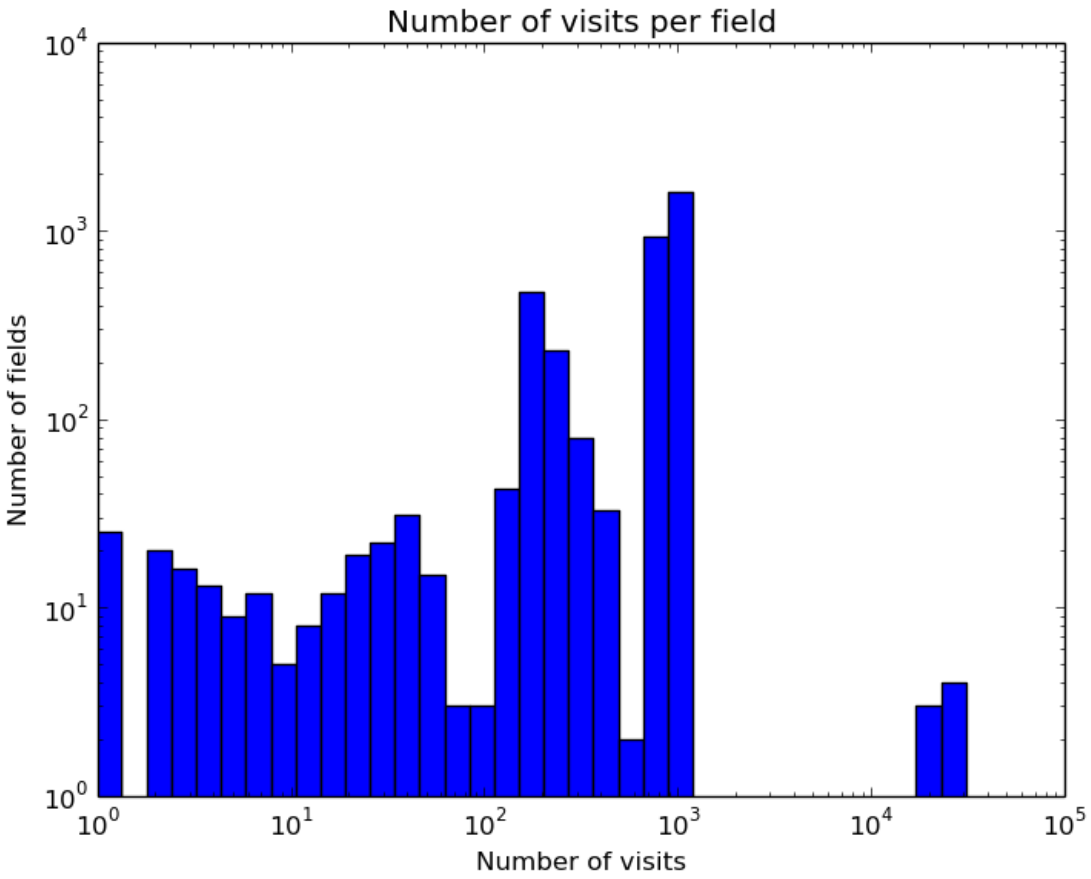

Figure 2.1: Distribution of number of visits per field for a single VRO operations simulation. Deep-drilling fields show as a peak at $\sim$ 25,000 visits, and most regular cadence fields are in a peak at $\sim$ 1000 visits.

the rate of transiting exoplanet detection by VRO as a function of year of observation for transiting hot Jupiters, hot Neptunes, and hot Super Earths.

2.2 Methods

Here we describe the methods by which we generate simulated VRO light curves, list the fiducial transiting exoplanet systems that we will analyze throughout this work, describe how we inject simulated transits of these exoplanets into the simulated light curves, and describe the period-search methods we use to probe the detection of the transits in the simulated light curves.

2.2.1 Simulated Light Curve Generation

We create simulated light curves using the method described in Lund et al. [26], Jacklin et al. [21] which we summarize here. Each light curve depends on five parameters: host star mass, radius of transiting planet, distance of the system from Earth, period of transiting planet, and VRO cadence (i.e. regular or deep-drilling). Each of the systems simulated assumes circular orbits with equatorial transits (i.e., we do not consider the effects of orbital eccentricity or grazing transits).

All host stars in our simulations (see Section 2.2.2) are dwarfs with spectral types determined via mass interpolation from Table 15.8 in Cox and Pilachowski [15], absolute magnitudes per VRO filter from Covey et al. [14], and radii derived using the mass-radius relationship from Beatty and Gaudi [4]. With this information, we create continuous and noiseless light curves. We then inject a simple boxcar transit into each of the light curves with a duration based on the planetary orbital period and stellar radius, and a depth dependent on the ratio of the stellar to planetary radii. In this analysis we assume circular orbits with equatorial transits, as well as noiseless stellar hosts.

With continuous light curves for a range of stellar radii, spectral types, planet radii, and planet periods (see Section 2.2.2), we time-sample them using the VRO operation simulation (OpSim) v2.3.2 run 3.61. The OpSim simulates ten full years of VRO observations considering factors such as weather variations and downtime for telescope maintenance. Out of the many parameters available from OpSim, we utilize time of observation, filter, and limiting magnitude. Based on our previous findings that the vast majority of transiting exoplanet detections will occur in the deep-

drilling fields [26, 21], we therefore consider only the deep-drilling cadence from the OpSim.

Once a light curve has been simulated we sample it and place our planet-star systems at a chosen distance and calculate the star's apparent magnitude in VRO's g, r, and i bands, which exhibit the least random photometric noise as shown in Lund et al. [26]. We then calculate the expected total per-visit photometric precision per VRO band using the stellar apparent magnitude with:

$$\sigma_{tot}^2 = \sigma_{sys}^2 + \sigma_{rand}^2 \,, \tag{2.1}$$

as described in Ivezic et al. (2008). We take σ_{sys} as the system designed noise floor of 0.005 for each band. The random photometric noise σ_{rand} varies with respect to a band-specific parameter (γ) and the apparent magnitude, and is calculated by:

$$\sigma_{rand}^2 = (0.04 - \gamma)x + \gamma x^2 \,, \tag{2.2}$$

in which $x = 10^{(m-m_5)}$ where m_5 is the 5σ limiting magnitude per VRO filter. The value of m_5 is generated by OPSIM and changes each visit based on sky brightness, seeing, exposure time, airmass, atmospheric extinction, and instrument throughput [20]. We add noise to the light curves on a per-band basis in order to simulate observed S/N. The random noise tends to be largest in the u, z, and y filters, and main sequence dwarf stars tend to be intrinsically much fainter in those filters as well. We therefore discard the visits using the u, z, and y filters, since their larger noise makes them less useful for transit detection. In the final step we median-subtract each of the remaining light curves (those in the g, r and i filters) and combine them into one master light curve. Table 2.1 lists the absolute magnitude, total magnitude, and total noise as a function of VRO filter and band for each of our simulated systems described in Section 2.2.2.

We note that this treatment of noise in the light curves does not at present include the possible effects of contamination by neighboring stars, which could become important for crowded regions such as the Galactic plane, bulge, and possibly also the Magellanic Clouds. We defer a treatment

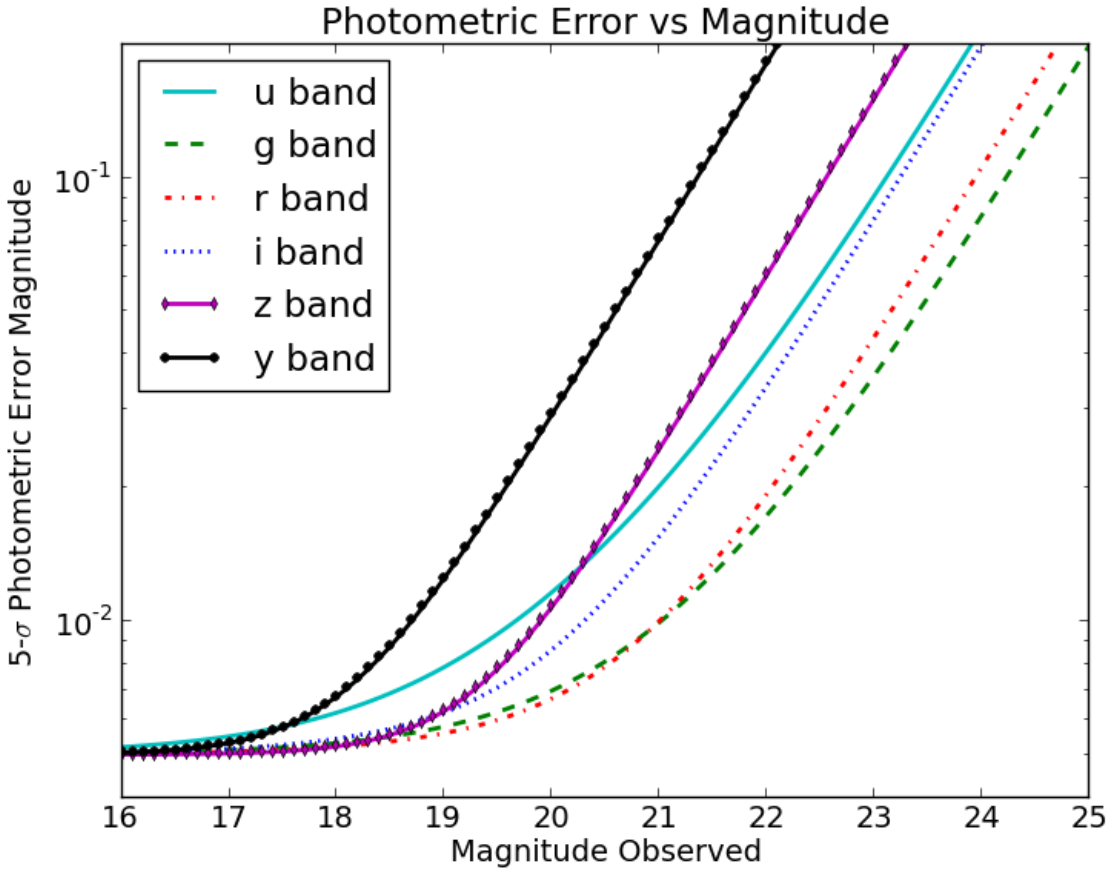

Figure 2.2: Per-visit VRO photometric error as a function of apparent magnitude for each filter from Lund et al. [26].

of this additional complication to a followup paper (Lund et al., in preparation), and for our current purposes emphasize that the approach laid out here applies, strictly speaking, to non-crowded fields.

We also do not attempt to simulate the possible effects of stellar noise (e.g., activity). As described in the following section, we have selected transiting planets to simulate that would result in relatively large transit signals of $>1\%$, which should not be significantly affected by typical activity levels on most solar-type stars [3]. Typical activity levels on M-dwarfs could be more important. For the purposes of this work we simply caution that our simulations of transiting planets for M-dwarfs apply in the case of relatively inactive stellar hosts.

2.2.2 Example Exoplanet Systems Simulated

In order to explore a representative range of results, we simulate several different exoplanet systems. We begin with the fiductal systems from Lund et al. [26], Jacklin et al. [21], namely, a hot Jupiters with radii of $5-14R_{\oplus}$ orbiting a $1M_{\odot}$ G-dwarf host star at 7 kpc. In addition, we simulate a hot Neptune with a radius of $6R_{\oplus}$ orbiting a $0.6M_{\odot}$ K-dwarf at 2 kpc, and a hot Super-Earth with a radius of $2R_{\oplus}$ orbiting a $0.25M_{\odot}$ M-dwarf at 200 pc. Each of these cases was chosen specifically to fit within VRO's expected parameter space (i.e., within the detection and saturation limits of all filters; see Fig. 2.3) [27]. The planet radii were selected to create an approximate 1% drop in total stellar flux as observed from Earth.

The quality of light curves generated for exoplanet detection primarily depends on the number of points included, which for VRO is $\sim$1000 points for objects in regular fields and $\sim$10000 for objects in deep drilling fields. Depending on the brightness of the system's host star, some bands will not be useful for exoplanet detection, and therefore it is important to understand how many of the observations taken in a deep-drilling field will actually be useful. We can parametrize detectability by photometric RMS precision, according to the absolute magnitude (determined by stellar mass) and the distance to the star, thus yielding the apparent magnitude. This is then used to calculate expected RMS precision via the methods discussed in in 2.2.1. We then exclude all

Mass ($M_\odot$)	Filter	Abs Mag	App Mag	Total Noise (mag)
1.0	*g*	5.84	20.07	0.01
1.0	*r*	4.47	18.70	0.01
1.0	*i*	4.31	18.54	0.01
0.6	*g*	10.21	24.44	0.02
0.6	*r*	7.65	21.87	0.02
0.6	*i*	7.10	21.33	0.12
0.25	*g*	14.41	28.63	5.54
0.25	*r*	11.31	25.53	0.43
0.25	*i*	9.72	23.94	0.19

Table 2.1: Absolute magnitude, total magnitude, and total noise as a function of VRO filter and band for each of simulated system.

observations for a given star for which the precision is worse than 30 mmag, a fiducial precision that will be investigated in detail in later work.

We wish to examine what types of stars will be most suitable for transit searches in VRO deep drilling fields. Figure 2.3 shows the number of observations that VRO will take, over 10 years, of a given object at deep drilling cadence (i.e., its sensitivity) where the noise is less than 30 mmag per observation. The colored limits in Figure 2.3 are defined by the saturation and detection thresholds of VRO.

2.2.3 Recovery of Simulated Planets

2.2.3.1 Period Search with Box-fitting Least Squares

The principal metric in this study is the recoverability of the period of the simulated planet transits and the recovered period's associated power. For this purpose, we utilize the standard BLS algorithm [24] as implemented in the VARTOOLS software tool [19].

We first examine how well BLS is able to recover a sample transiting planet. First, we generate 1000 simulated light curves of a typical Hot Jupiter. This system consists of a solar-type star (1 $M_\odot$, 1 $R_\odot$) with a $10R_\oplus$ planet in a 4.2-d orbit. We place the star at 7 kpc from the Earth, in order to situate it at a distance where the apparent magnitude of the star is near the bright end of the VRO magnitude regime. The 1000 simulated light curves represent 1000 realizations of the VRO noise model and in each we randomize the orbital phase of the planet transit.

We run BLS on each light curve and compare the top period returned by BLS (as measured by the BLS signal to noise ratio) to the input period. Figure 2.4 shows a histogram of the resulting periods for the 1000 realizations, using light curves with regular VRO cadence (*a*) and the deep drilling cadence (*b*). For this initial test case, we see that BLS recovers the correct input period with an accuracy of 0.1% in at least 25% of cases for regular cadence and at least 91% of cases for deep drilling cadence.

Aside from the question of recovering the transit periods correctly, an important issue for VRO will be identifying the transits with some measure of statistical confidence over various types

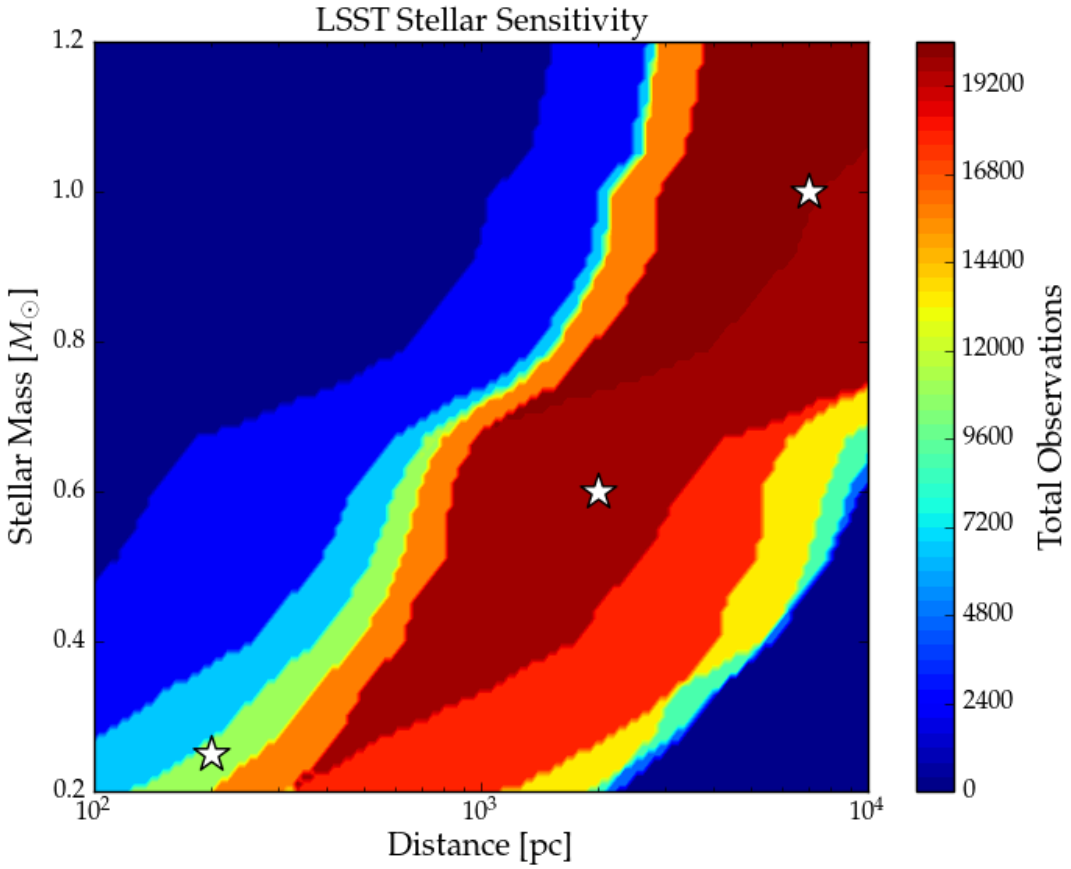

Figure 2.3: This figure displays, for a given stellar mass and distance, how many observations will be of sufficient precision (< 30 mmag) in a DD field to permit exoplanet detection after 10 years of operation. Warm colors indicate a large number of observations over several VRO bands, and cooler colors indicate fewer observations with sufficient precision. White stars indicate the stellar systems we explore in this paper. There are ∼20,000 total deep-drilling observations in OpSim v2.3.2 run 3.61, although the typical numbers discussed in the past for the DD fields have been roughly 10,000 observations [20] due to the ongoing development of the instrument and simulation techniques.

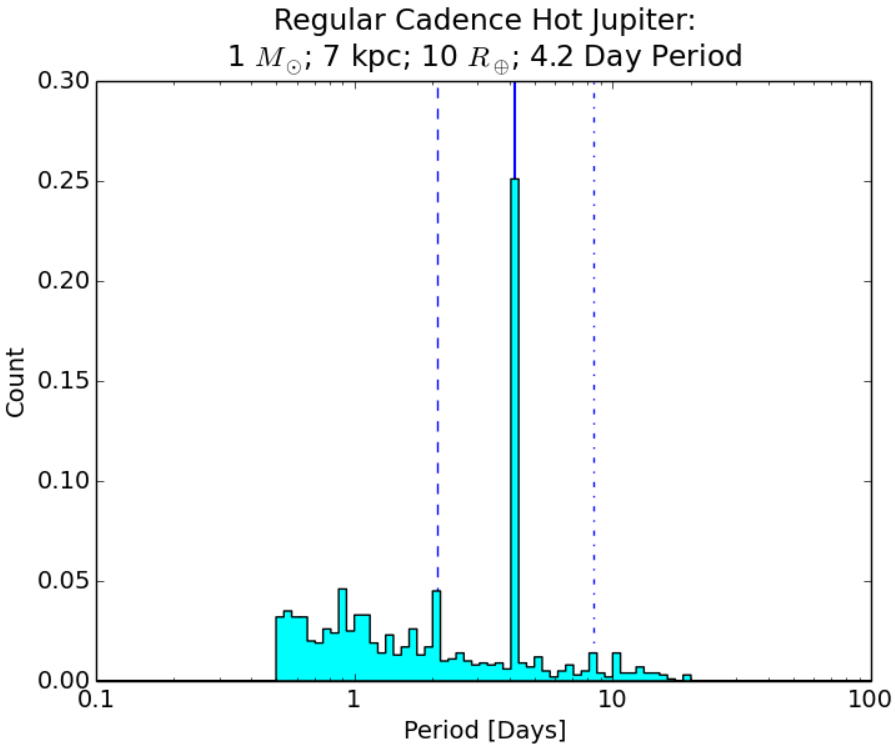

.45

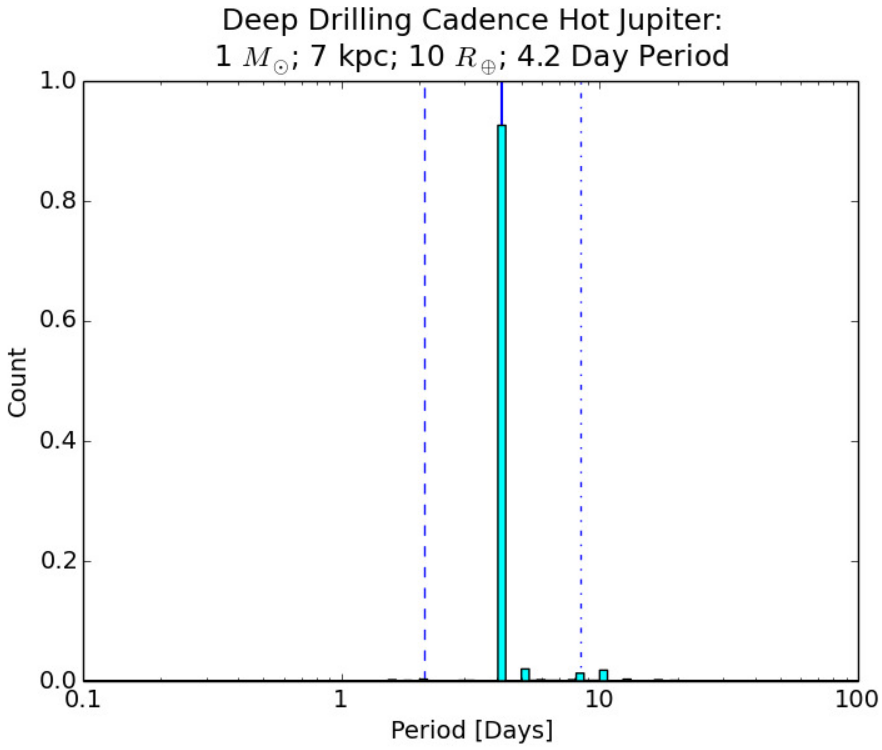

.45

Figure 2.4: Normalized histograms depicting the top BLS recovered period for a $10R_\oplus$ *hot Jupiter orbiting a one solar mass star at 7 kpc from Earth with a 4.2 day input period, for regular cadence (left) and deep drilling cadence (right). The bold vertical line marks the input period, and the two dashed lines on either side mark the half and double period.*

of false positives. For many transit surveys, astrophysical false positives are most important to eliminate [11]. Those will be extremely important for VRO transit searching, but in this paper, we focus only on photometric false positives, where the photometric noise randomly produces transit-like features in light curves. Assuming Gaussian photometric noise, we can quantify how well the BLS power can distinguish a real input transit signal from a photometric false positive at a given confidence level.

Figure 2.7 examines the distributions of BLS power for simulated transits (blue and green histograms) versus the "null" case of light curves without any injected transits (red histogram). Because our simulations involve 1000 simulated light curves, the maximum BLS power in the 1000 null light curves in essence represents the power above which we can expect a photometric false-positive probability of $<0.1\%$. In the case of a regular cadence field (left panel), we find that light curves with correctly recovered periods have, on average, higher BLS power than light curves for which the correct period is not recovered or for the null case, as expected. However, only 7% of all regular cadence light curves have correct periods recovered with a BLS power above the 99.9% confidence threshold defined by the null case. Clearly, photometric false positives will be a serious concern for regular cadence fields, at least using the BLS criteria we have examined here.

The situation is much improved, however, in the deep drilling cadence. Here, 98% of light curves with correctly recovered periods having BLS power above the 99.9% confidence threshold. From this simple analysis we see that the deep drilling fields not only recover the correct period at a higher rate, but also that a much larger proportion would survive a very simple cut on BLS power to exclude photometric false positives.

For this work, we perform the BLS period search in all cases over the period range $0.5 \leq P \leq 20$ d. We implement BLS on each of our simulated light curves for each system architecture (see Section 2.2.2). To probe the likelihood of exoplanet detection with the accumulation of VRO data over time, we apply the BLS detection algorithm to each simulated light curve 10 times, once each for elapsed time $\Delta t = [1, 10]$ yr from the start of VRO observations.

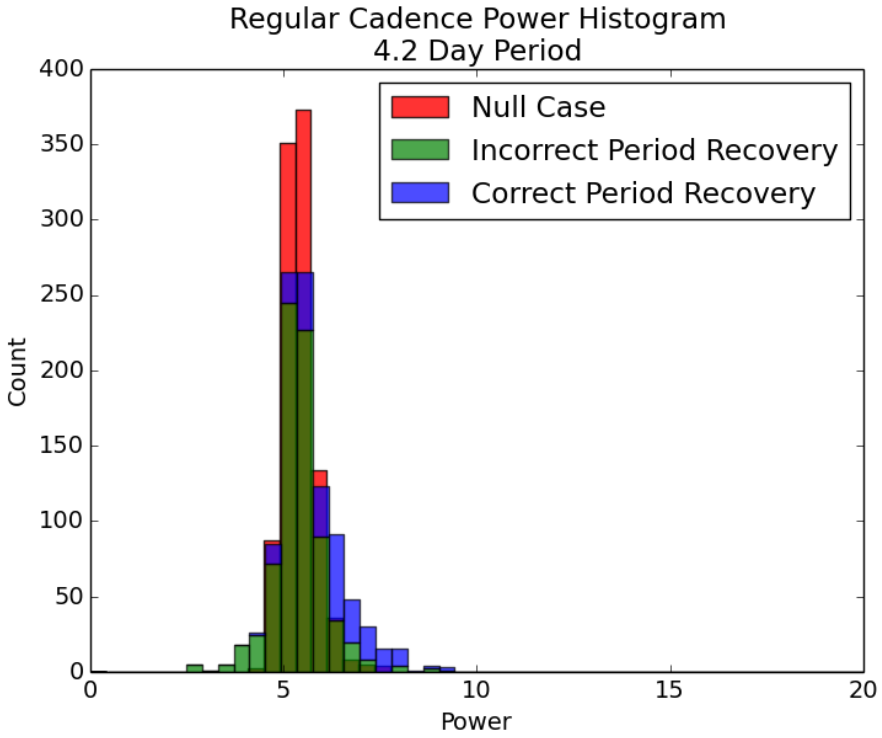

width=.5

Figure 2.5: Regular Cadence

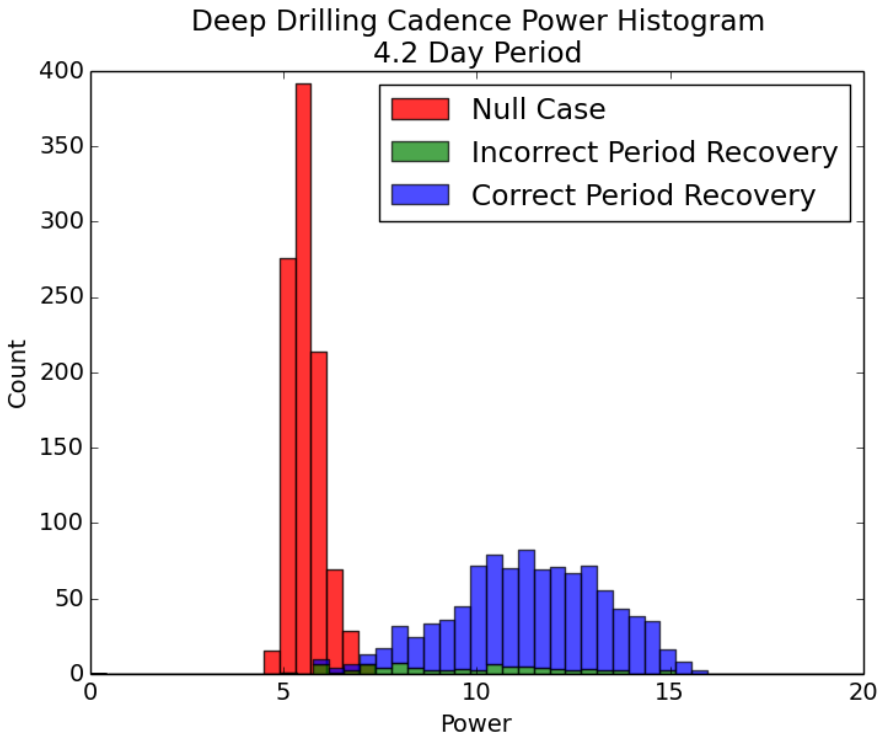

width=.5

Figure 2.6: Deep Drilling Cadence

Figure 2.7: Histograms depicting the power for the top BLS recovered period for a $10R_{\oplus}$ *Hot Jupiter orbiting a one solar mass star at 7 kpc from Earth with a 4.2 day input period, for regular cadence (left) and deep drilling cadence (right) with respect to the null case shown in red. Green represents cases where the correct period was not recovered, and blue represents cases where the correct period was recovered.*

2.2.3.2 Exoplanet Period Recoverability vs. Detection

In this work, we deem an exoplanet "recovered" if the top period returned by BLS is within 0.1% of the input period. An exoplanet is "detected" if the period is recovered and the false positive probability is less than 0.1%. The false positive probability varies by the number of years of accumulated data.

We calculate the false positive probability by creating an equivalent light curve with no injected transit for each cadence (i.e. regular or deep-drilling), stellar mass, distance, and year of observation. The resultant light curves are then run through BLS, which calculates the highest power peak returned by a non-transiting system. This process returns ten top values for the BLS powers, one for each year of observation, for a given stellar mass and distance combination. These values of the BLS power are used as a comparison template for each transiting system sharing the same stellar mass and distance: if the period of a transiting planet is recovered, and the BLS power of that period is greater than the false alarm probability, the planet is considered detected.

2.2.3.3 Mitigation of Diurnal Sampling

As a ground-based telescope, exoplanet detection using VRO will necessarily be affected by diurnal observing patterns. Jacklin et al. [21] showed that the effects of diurnal sampling specifically limit the detection probability at periods of integer and half-integer days. As a check, we finely sampled the range of periods from 4.9 days to 5.1 days with a resolution of 0.01 d for a $12R_{\oplus}$ planet orbiting a $1M_{\odot}$ star at 7 kpc over ten years of observation. Figure 2.8 shows the detection probability, with the expected drop in detection at a period of exactly five days. Based on the sharpness of this probability decrease we do not consider periods within 0.05d of integer and half-integer days for the remainder of this analysis. A similar sharp decrease in detection is exhibited at an integer sidereal day (at ~ 4.98 solar days); this feature is within 0.05d of the integer-day feature and thus is also excluded from the remainder of our analysis.

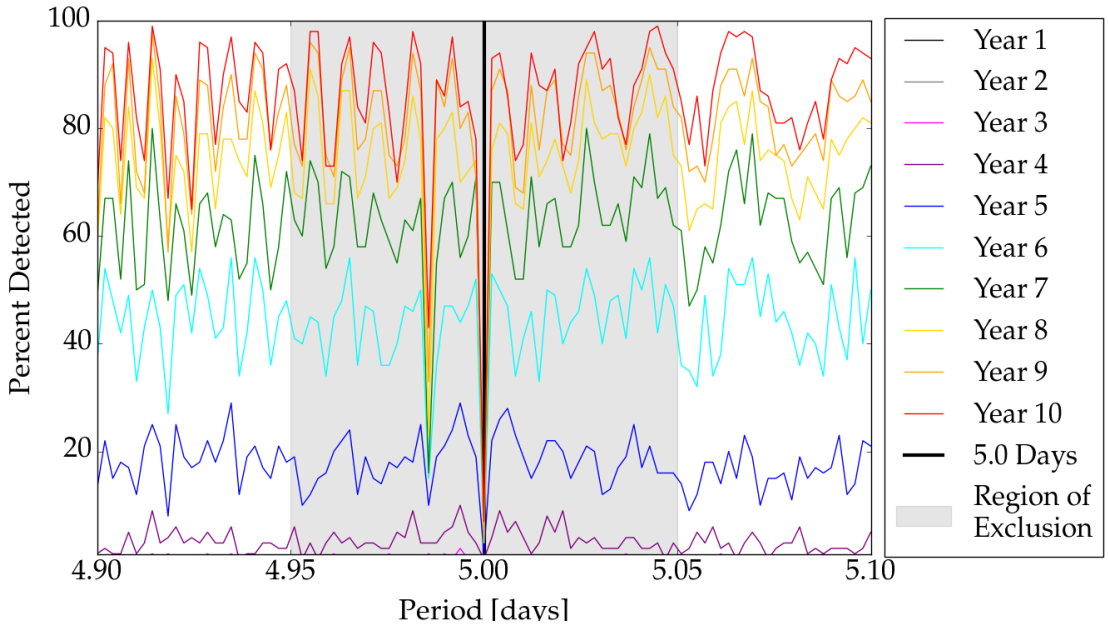

Figure 2.8: This figure shows a detection drop at period that is an integer multiple of 1 day (∼5 days) and 1 sidereal day (∼ 4.98 days) for a $1M_{\odot}$, $12R_{\oplus}$ transiting exoplanet system at 7 kpc. Points that fall within the region of exclusion (gray area) are below the time resolution of our later simulations. We therefore exclude parameter space within 0.05 d of integer and half integer multiples of 1 d from period searches for the remainder this study.

Chapter 3

Period Recoverability

3.1 Results

3.1.1 Period Recoverability of Exoplanets with VRO

We now apply our period recoverability test as in our Methods section to a broad range of planet radii and orbital periods for a fiducial star and system distance from Earth. First, we examine what fraction of planets are correctly recovered across a range of input periods for several types of planets. Second, we broaden that analysis to look at transit recovery across a range of period and radius parameter space. In all cases, we define a correctly recovered transit as one in which the period of the strongest BLS signal matches the input period to a 0.1% accuracy.

Our period recoverability analysis includes simulations of six different planets sizes, representing hot Jupiters with radii of 12 $R_\oplus$, 11 $R_\oplus$, 10 $R_\oplus$, hot Saturns with radii of 9 $R_\oplus$ and 8 $R_\oplus$, and a hot Neptune with a radius of 4 $R_\oplus$. In each case, we simulate the same host star representing a Sun-like dwarf with mass of 1 $M_\odot$ and radius of 1 $R_\odot$ at a distance of 7 kpc, and in each case we vary the planet orbital period over the range 0.5–20 d in increments of 0.1 d. For each of the exemplar cases, we create 1000 light curves for each input period, for both regular cadence and deep drilling cadence, as in Section 5.2.

The period recoverability results for the specific planet radii are shown in Figure 3.1, for both regular and deep drilling cadence, using vertical lines to emphasize detail at the integer and half-integer day periods. We also represent the results of period recoverability across period and radius space using two-dimensional histograms to convey the broader trends, as shown in Figure 3.5 (*a*) at regular cadence and Figure 3.5 (*b*) at deep drilling cadence. Warm colors such as red and orange indicate high fractional accuracy period recoverability and cool colors such as blue and green indicate lower fractional accuracy. We use the maximum power from the null cases displayed in

Figure 2.7 to establish a power threshold that represents detections with a photometric false positive rate $< 0.1\%$ using our current BLS detection algorithm. Irrespective of the power cut, we find that the deep-drilling fields exhibit substantially higher period recoverability rates, and with the power cut implemented there is only a small decrease in recoverability. This indicates that the current algorithms we are using would be sufficient to identify candidate transiting planet light curves. For regular fields, we find that while there is still a sizeable number of light curves that return the correct period, the power is often too low for us to identify them as candidates and we are only left with significant number of detections for very large planets with very short periods. There will be a very large number of light curves that the regular fields will contain, and any improvements in candidate selection using a more sophisticated algorithm to identify planet candidates will result in an increase in planet yield. These improvements will also likely include increasing the parameter space that is being reliably explored by extending it to longer periods and smaller radii. Examining how best to improve our current algorithm will be an interesting question for future work.

As expected, the results are similar to previous calculations of transit recoverability [47, 13], with strong biases towards greater recoverability for large planets and short periods. The larger number of observations with deep drilling cadence significantly increase the recovery rates. In particular, in the standard cadence the recoverability is strongly affected by planetary radius. Inflated Hot Jupiters ($R > 11R_{\oplus}$) exhibit recoverability greater than 50% out to periods of $\sim$4 days. Non-inflated Hot Jupiters and Saturns are recoverable out to $\sim$2 days. Hot Neptunes are essentially undetected, with a maximum recoverability of $\sim 2\%$ at a 1-d period. The deep drilling fields are quite different. Large giant planets ($R > 7R_{\oplus}$) are recoverable at a rate of greater than 60% out to periods of 10 days, and at rates from 30% to 50% out to at least 20 days. For small planet sizes of $R \approx 6R_{\oplus}$, the recoverability drops quickly, and only short period ($P < 5$ d) planets are recovered.

In all cases, we also see that the period sensitivity is strongly influenced by the diurnal sampling, showing sharp declines in sensitivity at integer and half-integer day periods, which is not surprising. Interestingly, however, while the window function results in drops in period recoverability at integer and half-integer periods when the average period recoverability is high, there are

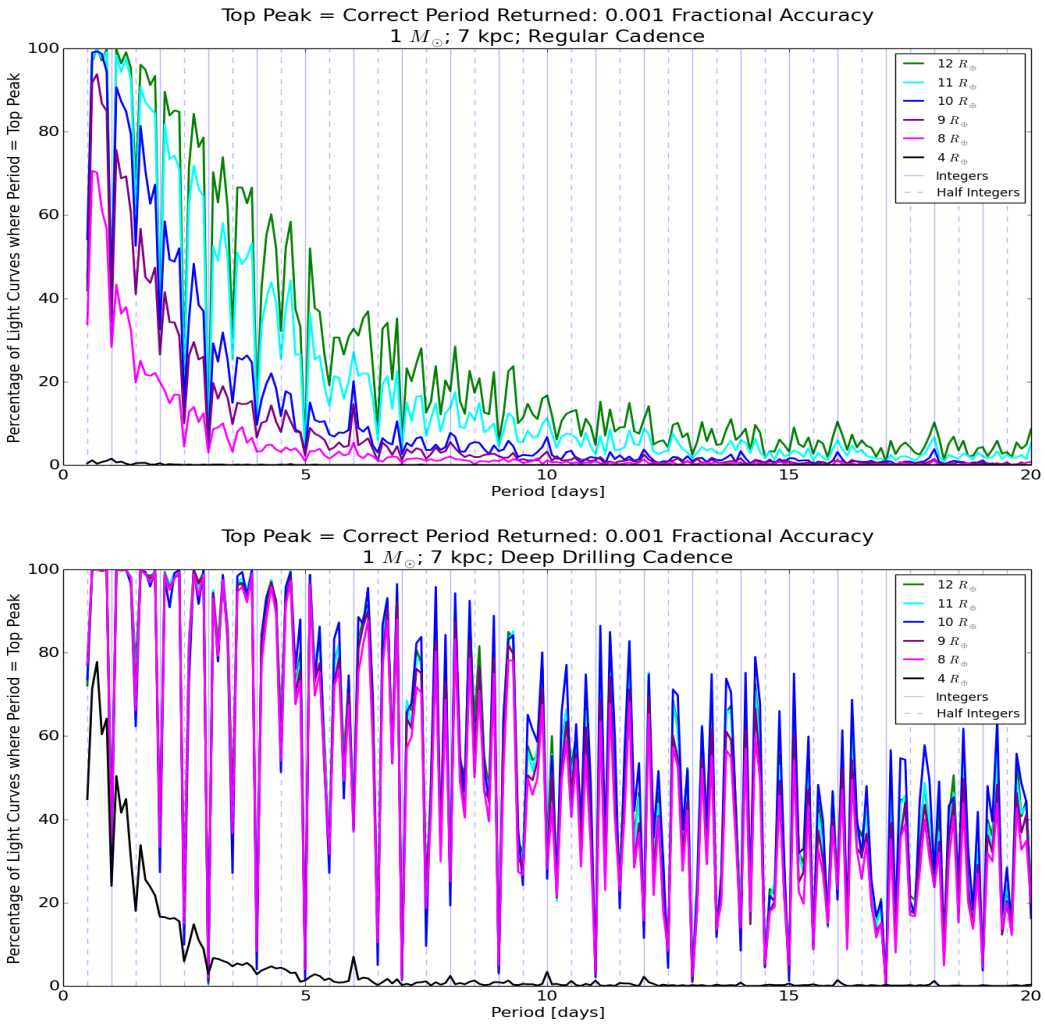

Figure 3.1: Regular (top) and deep drilling (bottom) cadence period recoverability of 4, 8, 9, 10, 11, 12 $R_\oplus$ transiting exoplanets about a 1 $M_\odot$ star at 7 kpc. The larger the planetary radius and the shorter the period, the more likely it is that BLS will recover the top period. Period recoverability is much more accurate at deep drilling cadence than at regular cadence, with significant recoverability exhibited for most tested planetary radii out to 20 d periods and beyond.

actually increases in recoverability at the integer and half-integer periods when the average period recoverability is very low (e.g., black curve in Figure 3.1). This is because there is an increase in the number of observed transits for some planets when the period is at a half- or full-day integer, such that transits all occur at night when VRO can observe.

We also analyze deep-drilling period recoverability of a planet in the Large Magellanic Cloud. We simulated an inflated Hot Jupiter with a radius of 14 $R_\oplus$ around a $1M_\odot$ star at 50 kpc, and we use only the *g* filter which has the lowest photometric noise (Fig. 2.2). The resulting recoverability is shown in Fig. 3.6, which clearly shows that extragalactic planet recoverability is possible using VRO for such a system [21].

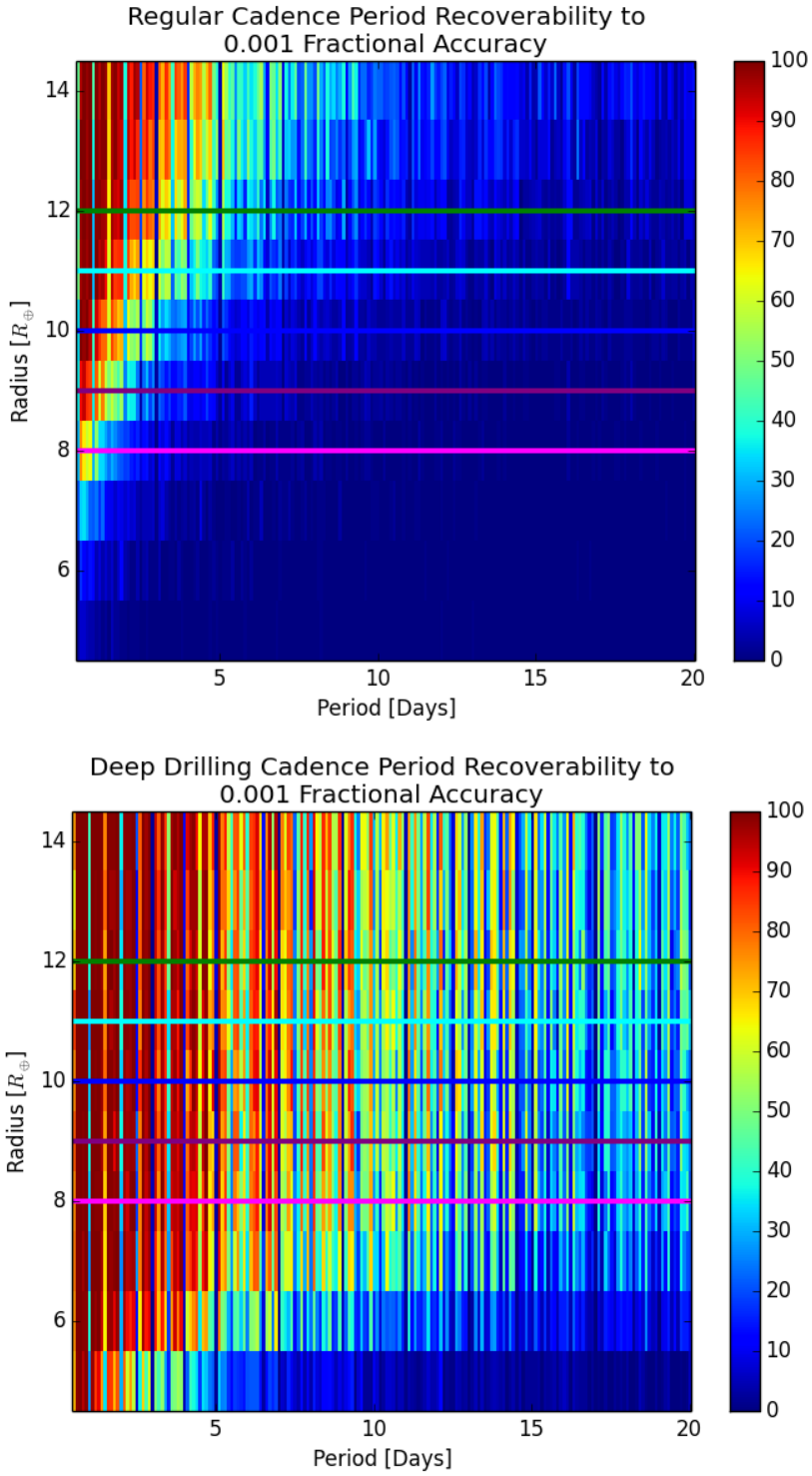

Figure 3.2: Two-dimensional histograms representing period recoverability considering only top BLS peak accuracy. Warm colors indicate high recoverability and cool colors indicate lower percentage recoverability. Deep drilling cadence (bottom) exhibits considerably higher recoverability in both period and radius space than regular cadence (top). Colored horizontal lines designate radii which are represented in Fig. 3.1.

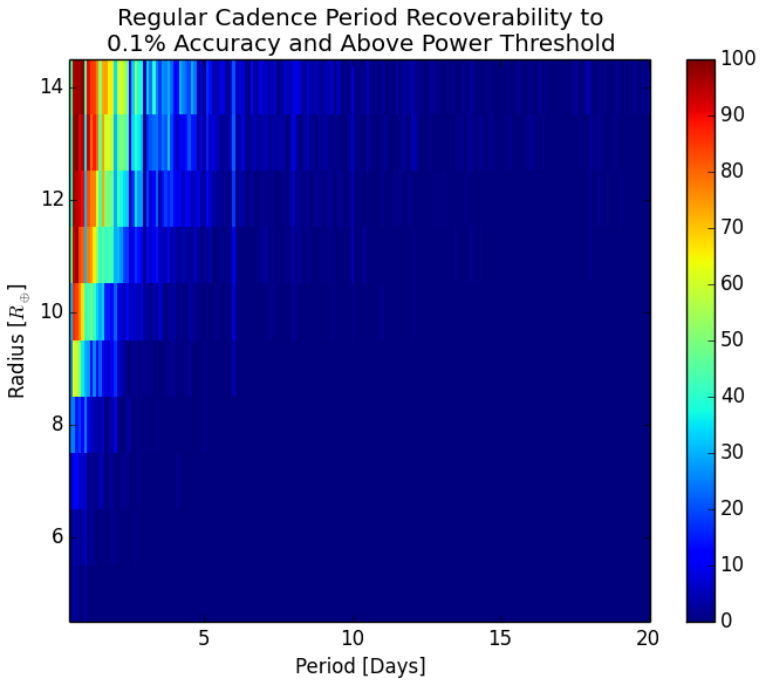

Figure 3.3: Regular Cadence

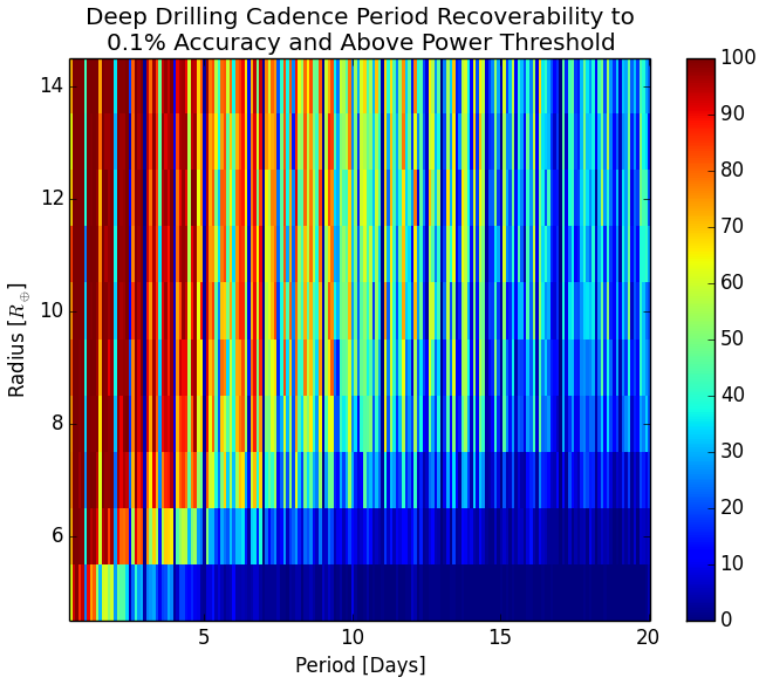

Figure 3.4: Deep Drilling Cadence

Figure 3.5: Period recoverability considering top BLS peak accuracy and power threshold where all detections have a BLS power greater than 7.69526 for regular cadence and 7.32893 for deep drilling cadence. Warm colors indicate high recoverability and cool colors indicate lower percentage recoverability. Deep drilling cadence (bottom) exhibits considerably higher recoverability in both period and radius space than regular cadence (top).

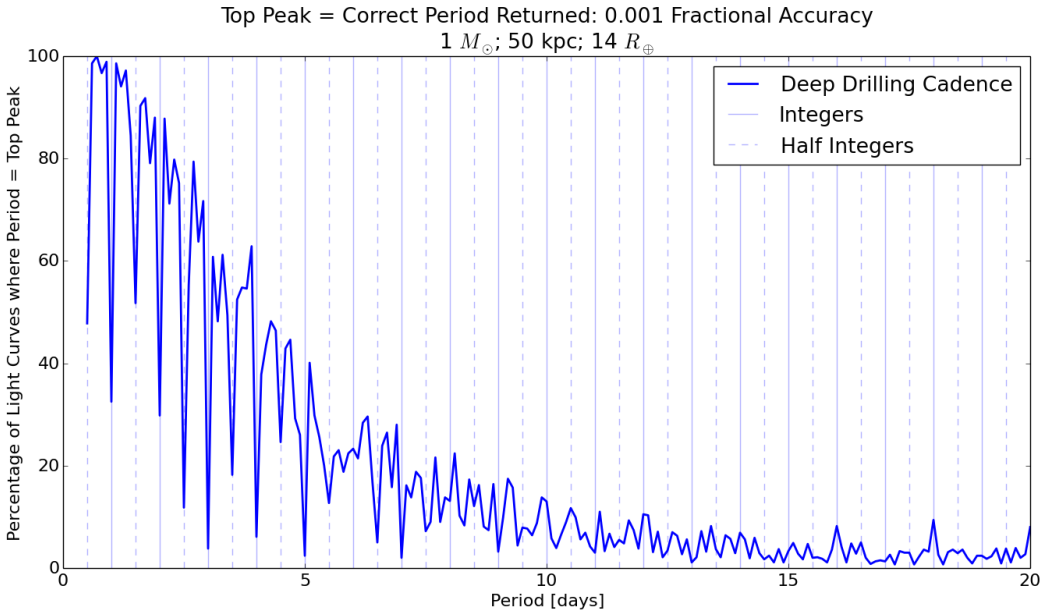

Figure 3.6: Deep drilling period recoverability for a 14 $R_\oplus$ Hot Jupiter about a 1 $M_\odot$ star at 50 kpc. This simulation exhibits VRO's period recoverability potential in the Large Magellanic Cloud.

Chapter 4

Exoplanet Detection with VRO

We have thus far demonstrated that period recoverabilty of exoplanets with VRO is successful. Therefore, when analyzing how quickly VRO will be able to deliver actionable results, we consider full exoplanet detection (as opposed to simple period recoverability) which is discussed in Section 2.2.3.2. For exoplanet detection, we only consider simulated observations from VRO's deep drilling fields since their more heavily populated light curves are much more likely to exhibit exoplanet detection than fields observed only at regular cadence. From here we also mitigate the effects of diurnal sampling by removing integer and half integer days as described in Section 2.2.3.3. In this section, we present the resulting transiting planet detection probabilities as a function of time for each of the three fiducial cases: a $10R_\oplus$ hot Jupiter orbiting a $1M_\odot$ G-dwarf at 7kpc, 4 and $6R_\oplus$ hot Neptunes orbiting $0.6M_\odot$ K-dwarfs at 2kpc, and a $2R_\oplus$ hot Super Earth orbiting a $0.25M_\odot$ M-dwarf at 200 pc.

4.1 Hot Jupiter Detection

The most successful exoplanet detection in the region of parameter space tested occurred with large planets orbiting a $1M_\odot$ host star at 7 kpc (see Figure 2.3). Here we tested a $10R_\oplus$ transiting exoplanet (Figure 4.1), representing the original system analyzed for period recoverability in Jacklin et al. [21]. As shown by the logarithmic shading in Figure 4.1, the large size of the transiting exoplanet yields a high probability of detection. Appreciable detection at very short periods ($<$ 3 days) is seen after about 4 years of observation, with excellent detection probabilities all the way out to 20-day periods after ten full years of observation. This overall pattern is summarized in Figure 4.2.

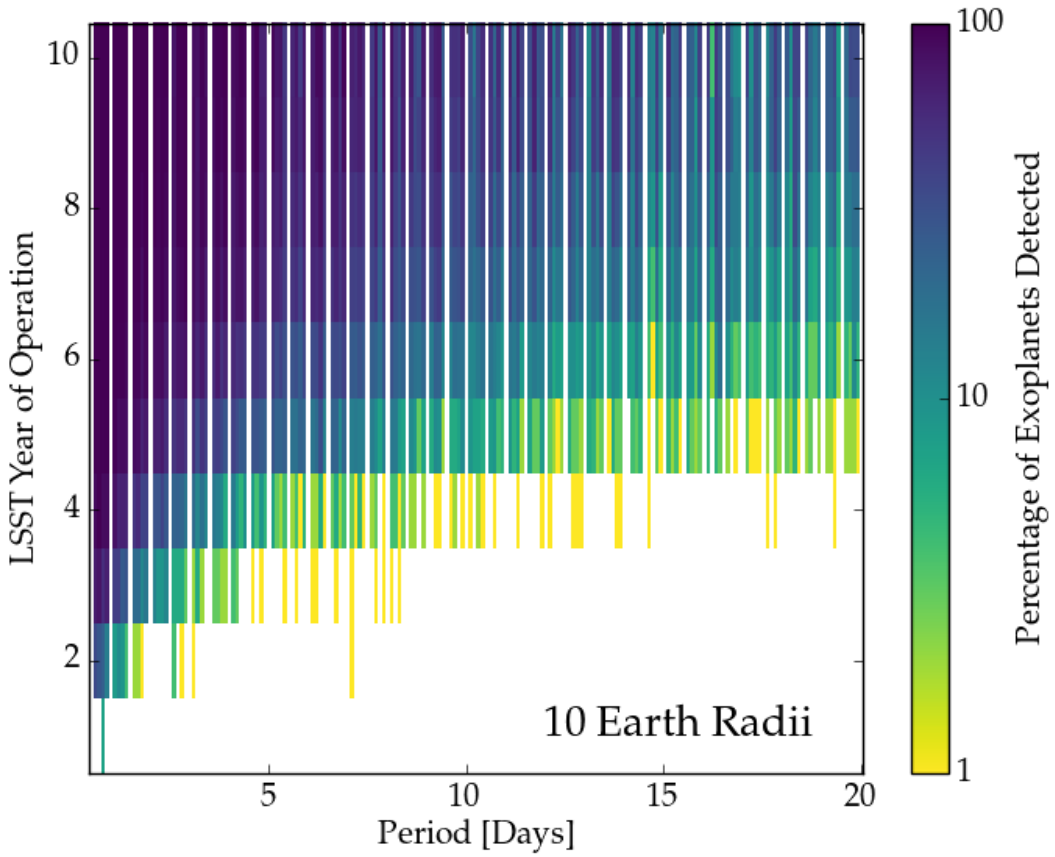

Figure 4.1: Two-dimensional histogram across orbital period and year of observation for a G-dwarf located in a deep-drilling field. This figure shows the results of simulating a $10R_{\oplus}$ transiting hot Jupiter at 7 kpc. The logarithmic color bar indicates the percent of total cases where the period of the planet is recovered to within 0.1% accuracy with an accompanying power that crosses the power threshold for a null transit of the same system. Periods at integer and half-integer days are removed in order to mitigate the effects of diurnal sampling.

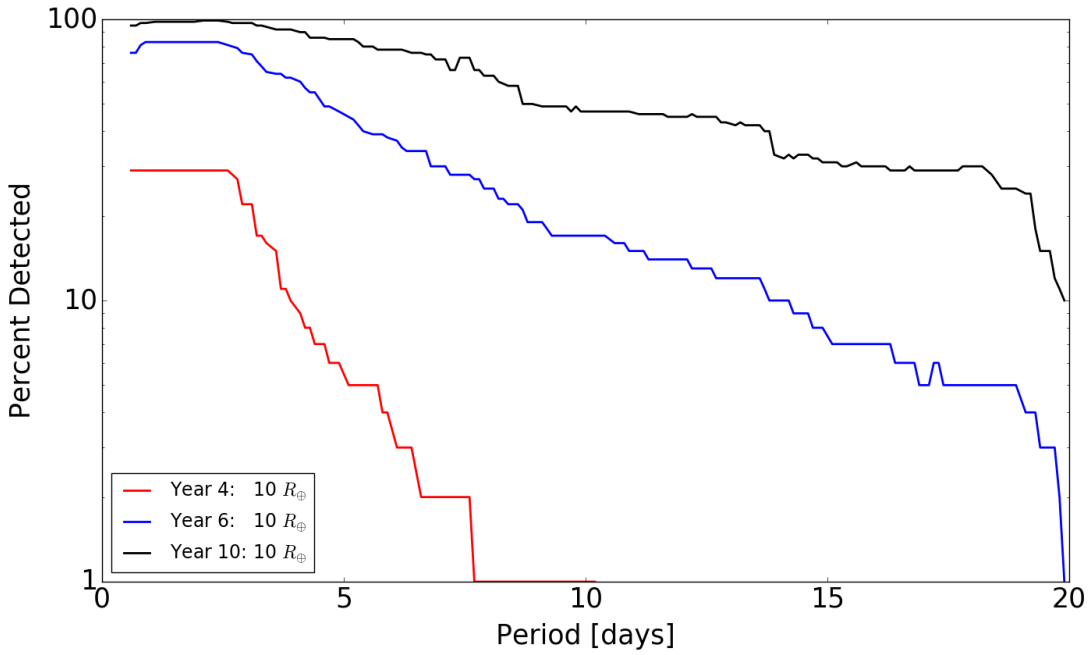

Figure 4.2: Detection probability as a function of orbital period for a G-dwarf with a 10 $R_\oplus$ transiting exoplanet at 7 kpc, based on light curves after 4, 6, and 10 years of VRO operations. The detection curves have had integer and half-integer periods removed, and are smoothed over a 3-day window.

4.2 Hot Neptune Detection

Results for a hot transiting Neptune-sized planet are also promising. We analyzed a $6R_\oplus$ planet and a $4R_\oplus$ planet transiting a $0.6M_\odot$ K-dwarf at 2 kpc (Figure 4.3). Detection of the $6R_\oplus$ exoplanet is high out to roughly 8-day periods after seven years of observation, with detection probabilities increasing with further years of observation. Detection of the $4R_\oplus$ exoplanet is more difficult, with high detection occurring only at $<$ 3-day periods after seven years of observation. This overall pattern is summarized in Figure 4.4.

4.3 Hot Super Earth Detection

The final system analyzed is a $2R_\oplus$ transiting exoplanet orbiting a $0.25M_\oplus$ M-dwarf at a distance of 200 pc. This system is the most Earth-like of the examples considered here and could potentially represent a rocky planet in an optimistic habitable zone as mentioned by Selsis et al. [38] and defined by Kasting et al. [23] at the fringes of our exoplanet detection space as defined by number of observations in Figure 2.3. The $0.25M_\oplus$ system at 200 pc represents an extreme in the VRO parameter space for transiting planet discovery as it is the closest to Earth that an $0.25M_\oplus$ star can be located without nominally saturating the VRO detectors. As shown in Figure 4.5, exoplanet detection in this case is difficult but not impossible. For the tested system, there is a very high probability that we will be able to detect $2R_\oplus$ exoplanets at periods shorter than $\sim$ 3 days after $\sim$ 6 years. As the period duration increases, the detection probability drops dramatically as summarized in Figure 4.6.

4.4 Discussion & Conclusions

From this work, we find clear indications that VRO will be capable of period recoverabilty for many interesting types of transiting planets. For the majority of the survey carried out at the regular cadence, we have seen that it should be possible to correctly recover the period of $\sim$50% of Hot Jupiter ($\sim 10R_\oplus$) transits around solar-type stars at orbital periods of up to 3–4 d.

The deep drilling fields, while a much smaller portion of the planned VRO survey, have much greater potential for planet period recoverability. In those fields, we show that it should be possible

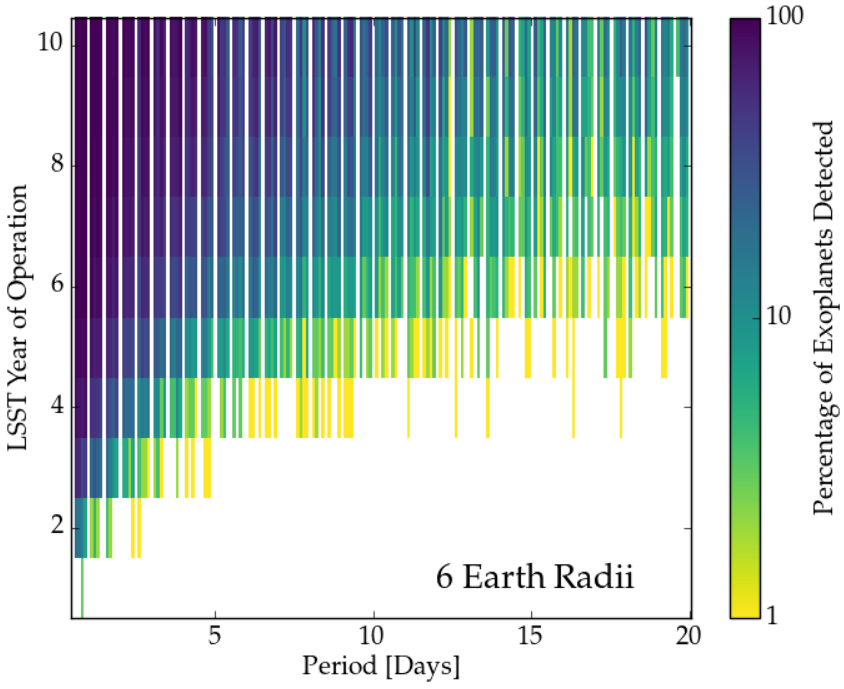

.45

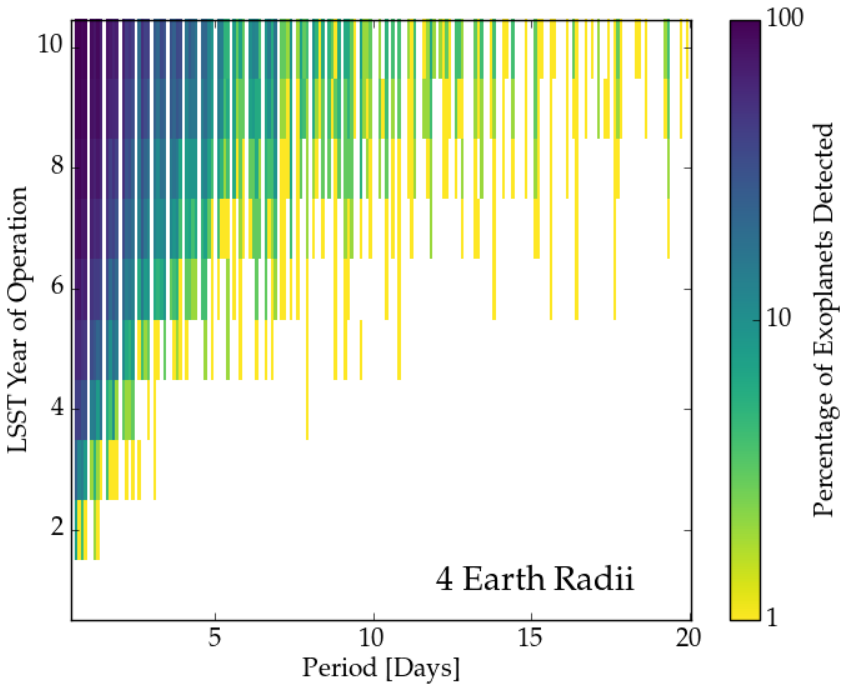

.45

Figure 4.3: Two-dimensional histograms across orbital period and year of observation for a K-dwarf located in a deep-drilling field. The top figure simulates a $6R_\oplus$ planet, and the bottom figure represents a $4R_\oplus$ planet, both utilizing a similar legend to Figure 4.1. Periods at integer and half-integer days are removed in order to mitigate the negative effects of diurnal sampling.

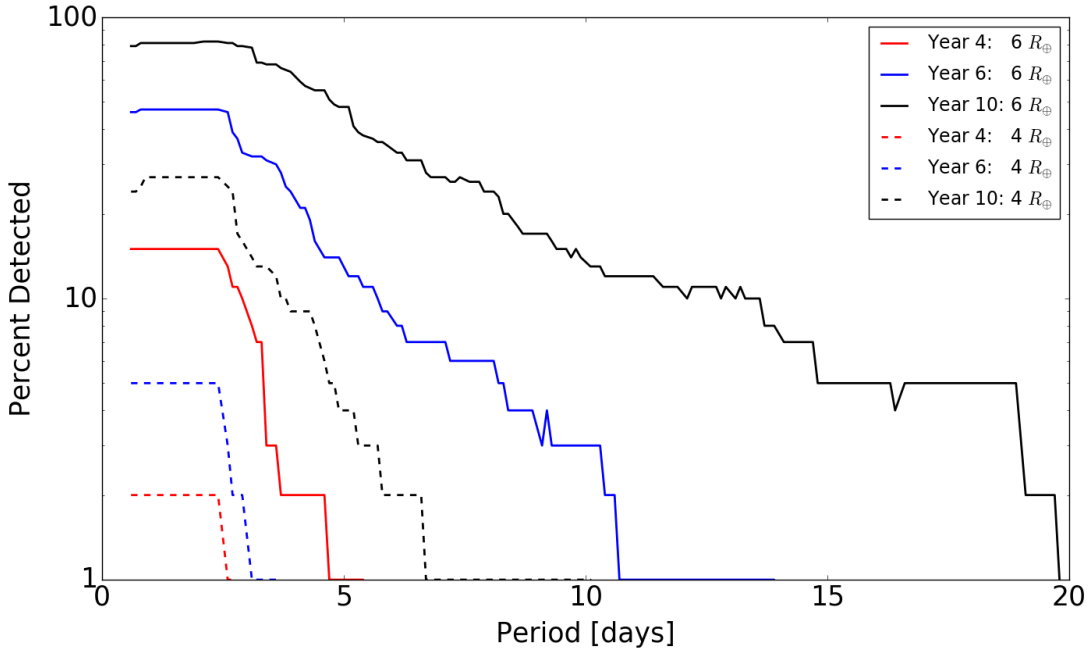

Figure 4.4: Detection probability as a function or orbital period for a K-dwarf at 2 kpc with a transiting exoplanet of 6 $R_\oplus$ (solid lines) and 4 $R_\oplus$ (dashed lines). The data have been processed in the same manner as Figure 4.2.

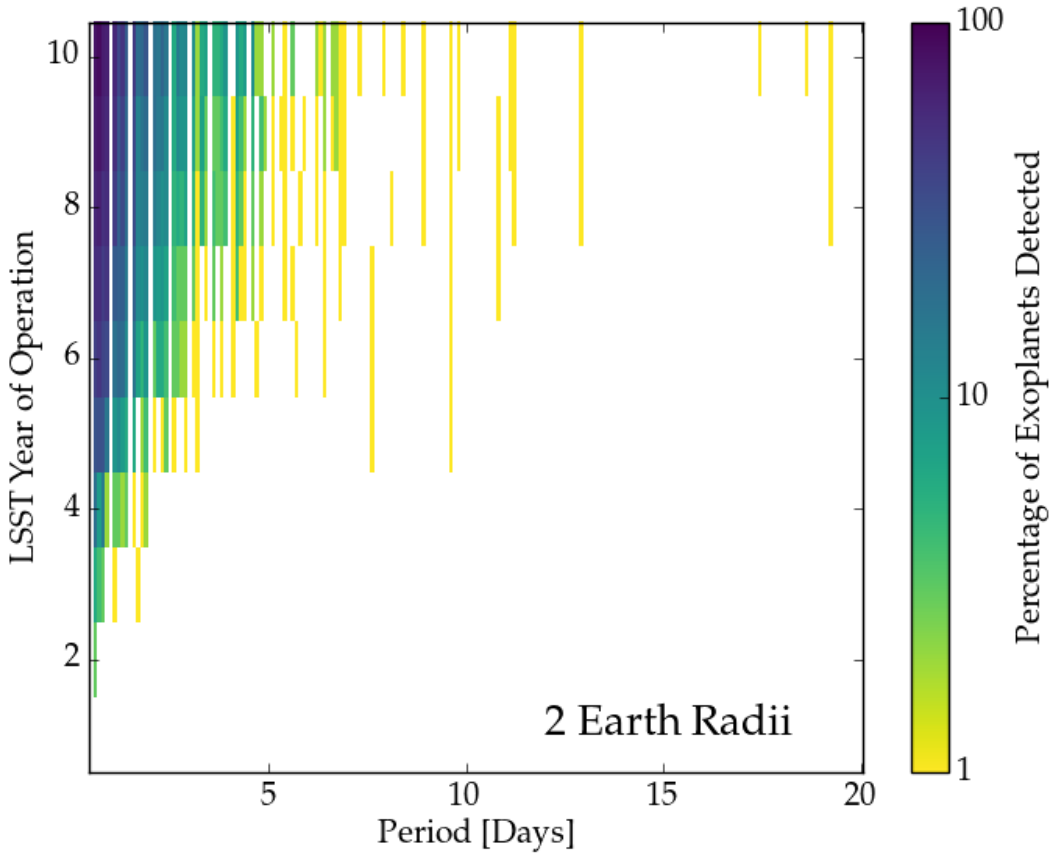

Figure 4.5: M-dwarf deep-drilling field two-dimensional histogram in period and year of observation space. This figure simulates a $2R_{\oplus}$ transiting hot Super Earth at 200 pc. This figure was created using the same data processing used for Figure 4.1 and Figure 4.3.

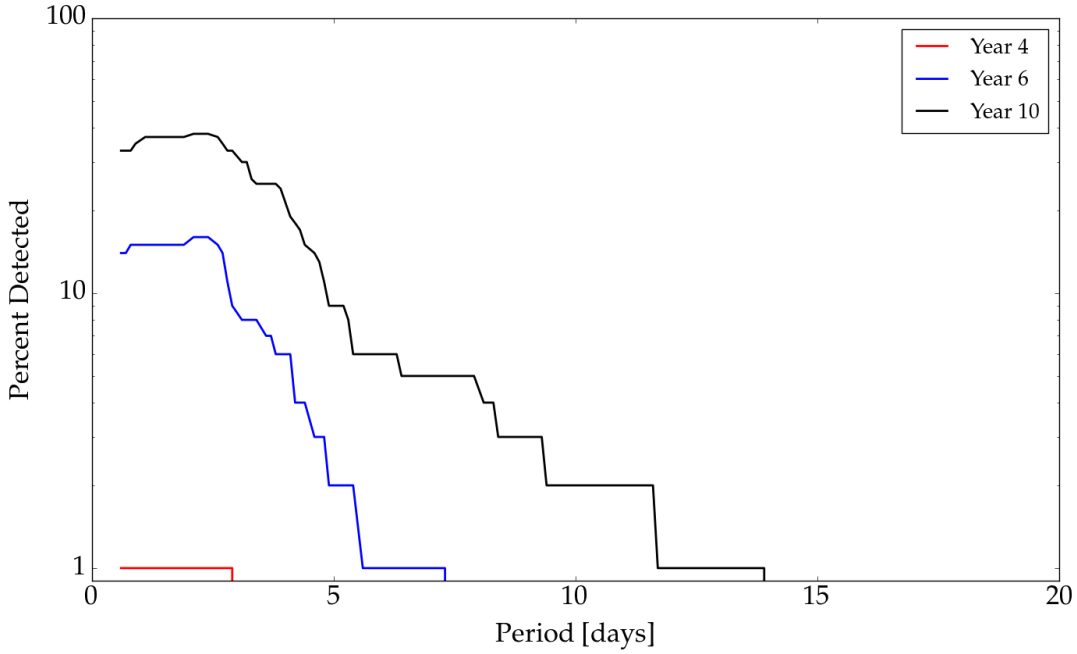

Figure 4.6: M-dwarf with at 2 $R_\oplus$ transiting exoplanet at 200 pc.The data have been processed in the same manner as Figure 4.2 and Figure 4.4

to accurately recover Hot Jupiters $\sim$40% of the time with periods as long as $\sim$20 d, the outer limit of our period search. We also find that in these deep drilling fields it should be possible to recover Hot Neptunes ($\sim 4R_{\oplus}$) with orbital periods of 1–2 d. While Hot Jupiters have been the most well-studied population of exoplanets, surveys such as *Kepler* have shown that Hot Neptunes are much more common, and thus represent a less well-studied population of exoplanets.

The second half of this work focuses solely on VRO's deep-drilling fields, as we have found that exoplanet detection is significantly improved by using deep drilling cadence as opposed to regular cadence. Additionally, since rapid results are of increasing importance as first light approaches, we examine not only what VRO will discover after its full tenure, but have also specifically explored exoplanet detection as VRO steadily accumulates more data. Indeed, this work has demonstrated that at least a few percent of the shortest-period ($<$ 2 d) hot Jupiters transiting G-dwarf stars and hot Neptunes transiting K-dwarf stars can be detected within the first 1–2 yr of VRO data collection (Figures 4.1 and 4.3). More generally, detection probabilities of $>$10% for periods $<$5 d are possible mid-way through the nominal 10-year VRO survey.

4.4.1 Discussion of Caveats

As expected, very short-period hot Jupiters transiting mid-type main-sequence stars (i.e., $1M_{\odot}$) are the easiest exoplanets that VRO will be able to detect, however they will be different from the systems explored by most other current surveys due to their faintness and distance from Earth. More generally, our work has shown that VRO will be capable of detecting a wide variety of exoplanets over a range of parameter space that is previously underexplored, including hot Jupiters at great distances and super-Earths around red dwarfs. Specifically, VRO will have the ability to probe planets orbiting distant and/or intrinsically dim stars ($r \sim 24.5$) over the entire southern sky. Finally, because the specific cadences and deep-drilling fields for VRO have not yet been fully defined, the work presented here may further help to develop optimal choices for the telescope.

Any detections that VRO makes will represent planet candidates – not confirmed planets. Due to the faintness of the stars that VRO will observe, traditional confirmation methods will likely

not be feasible. In both this work and Lund et al. [26], we have only shown that periodic transiting events can be recovered from VRO light curves. While this does show that the signal from a planet transit should be recoverable, it does not yet address the ability to differentiate between transiting planets and astrophysical false positives (such as eclipsing binaries). Our treatment of noise in the VRO light curves currently neglects both the effects of contamination (e.g., crowding) and of stellar variability (e.g., activity). Future simulations could attempt to estimate likely contamination ratios for different positions on sky, as has been done for the TESS Input Catalog [43], and could also include a random sampling of typical activity levels as a function of stellar spectral type. In addition, as shown in Section 5.2, for the regular cadence data in particular it will be challenging to disambiguate many or most of the types of transits we have simulated from statistical false positives, despite the accuracy with which the transit periods can be recovered. Our goal in future work will be to explore ways to differentiate between true transiting planets and other phenomena, as well as to investigate more robust methods for confidently identifying true transits in the regular cadence data. Additionally, we have also not attempted here to estimate the absolute number of transiting planets that may be discovered by VRO. To do this will require a comprehensive assessment of various types of false positives, which the additional capabilities described above would enable. Also, since follow-up observations which characterize VRO-detected planets in terms of atmospheric composition, thermal properties, or dynamics will generally not be an option, the main power of the detection of planet candidates will be to determine statistical populations. Learning how to correct the VRO planet candidate population for contamination by other astrophysical signals will therefore be crucial for statistical exoplanetary census studies.

4.4.2 Final Words on Transits with VRO

Here we have simulated several fiducial test cases that broadly explore VRO's exoplanet detection parameter space. As a next step we plan to more fully sample VRO's observational parameter space for transiting exoplanet detectability based on stellar mass, exoplanet radius, system distance, and exoplanet period for both VRO deep-drilling and regular cadence. It will also be useful

to consider the effects of eccentric orbits and grazing transits.

Most importantly, as we have demonstrated with a number of exemplar cases here, VRO should be capable of discovering a variety of exotic exoplanetary systems. In future studies we will examine the detection of planets at even longer periods, stellar hosts of different types and distances, and specific stellar populations. A more complete exoplanetary census will contribute to deeper understanding of the frequency, structure, and formation of these systems in our galaxy and beyond [22].

Chapter 5

Microlensing

5.1 Introduction

Gravitational microlensing occurs when a foreground "lens" star passes between the near-direct line of sight of Earth toward a more distant "source" star. The gravitational well generated by the lens star focuses the light from the source star to Earth, causing a characteristic magnification of source starlight over time (i.e. a Paczyński curve), sometimes to several orders of magnitude [31]. If the lens star has an orbiting planet, the alteration in the shape of the system's combined gravitational well changes the shape of the observed Paczyński curve, permitting determination of the exoplanet's properties.

Gravitational microlensing is currently the only exoplanet detection method available that is capable of probing the low-mass, long-period exoplanet population, and is therefore an important tool in determining an overall Galactic exoplanet census, mass function, and potential for habitability. Indeed, microlensing is in fact most sensitive to planets just beyond the so-called "snow line", and is the only exoplanet detection method that does not rely on light from the host star or planet in order to detect their presence [17]. Consequently, gravitational microlensing is able to detect planets around very dim stars (i.e. M-dwarfs), at large distances from Earth, and near the Galactic center. It is also the only way to detect non-self-luminous, free-floating planets, a population that is hypothesized to exist but has not yet been observed.

Gravitational microlensing is also challenging for a couple of reasons that often come into play at once. First, in order to beat the low intrinsic probability of individual short-lived microlensing events, there is a need for continuous photometric monitoring of large areas of the sky. Second, once detected, the often-complex behaviors observed in microlensing light curves lead to complexity in fitting analytic models. As a result, only a small number of microlensing planets have been discovered thus far, compared to the relatively large number of planets discovered by Doppler

and/or transit methods.

The Wide Field Infrared Survey Telescope (WFIRST) is the next NASA flagship mission prioritized by the 2010 Decadal Survey, scheduled to launch in the mid-2020s [18]. One of the primary science goals for WFIRST is using gravitational microlensing to complete a census of exoplanet demographics [42]. Maximizing the science yield of WFIRST for gravitational microlensing studies of exoplanets will depend on maximizing the number of microlensing events observed. Consequently, there is a need for precursor studies to identify the specific Galactic fields likely to yield the highest microlensing event rate within WFIRST's optimal brightness range.

This requirement for a maximal microlensing event rate implies fields that have maximal stellar densities on sky, i.e., the Galactic Bulge. However, not only do stellar counts increase, but also dust obscuration increases steeply toward the Galactic plane; thus, there is an intrinsic trade-off that requires careful study to determine the precise Galactic latitudes that are prime for WFIRST microlensing yields. Previous dedicated surveys of the Galactic bulge region, such as the Optical Gravitational Lensing Experiment (OGLE) [45] and Microlensing Observations in Astrophysics (MOA) [44], avoided the very center of the Galaxy (i.e., Galactic latitudes $|b| < 2^\circ$) because they operated at visible wavelengths, thus a detailed characterization of the highest stellar density regions toward the Galactic bulge remains to be done.

Indeed, Yee et al. [48] called for a ground-based near-infrared (NIR) survey to determine microlensing event rates in the potential WFIRST fields for the first time. In order to fulfill this goal, we have designed and implemented a 5-year photometric survey using the 3.8-m United Kingdom Infrared Telescope (UKIRT) located at the summit of Mauna Kea in Hawaii. Since UKIRT is able to observe in the NIR and is able to see through the dust at the center of our galaxy, its observational fields are able to lie closer to the center of the Galactic bulge than previous optical surveys. This observing strategy allows us to complete preliminary light-curve measurements in the NIR H and K bands, the same wavelength regions in which WFIRST will observe [39].

Section 5.2 first summarizes the UKIRT survey and its data products, and then describes the pipeline we have created to perform simulations of microlensing events and their recovery in the

UKIRT data. Section 5.2.4 provides an assessment of the validity of our simulations, and provides examples of the simulations' performance and challenges. We present our primary results in Section 5.3, including specifically the completeness of our microlensing event recovery as a function of stellar brightness, a (completeness-corrected) stellar luminosity function for the fields observed, and a determination of the intrinsic microlensing event rate for the fields observed. Section 4.4 discusses some of the limitations of the current work and our plans for future work. Finally, Section **??** presents a brief summary of our conclusions.

5.2 Data and Methods

5.2.1 The UKIRT Survey

This microlensing survey area is 10.5 $\deg^2$ and has a nominal duration of 5 years (2015–2019). All of the observations are focused on the Galactic bulge, and each field has a cadence of one to three observations per night. The closer the field is to the center of the Galaxy, the higher the cadence. We are observing the Galactic bulge in the H and K bands, and have chosen our fields to have some slight overlap with the OGLE and MOA surveys.

Figure 5.1 highlights the position of UKIRT's observational fields as well as their respective cadences. In 2015 and 2016, only the photometric NIR H-band was used in observations. In 2017, in addition to increasing the area covered by the survey, K-band observations were included in order to better constrain the microlensing source star colors. Multi-band observations are continued through 2018 and 2019, though our survey's strategy has since been adjusted to remove the northern fields that were observed in 2017. The choice to remove the northern fields was of dual purpose 1: the southern and northern fields show similar potential to event detection, and 2: this choice conserves monetary resources. Additionally, we drop approximately 2% of the survey's frames due to instrumentation or weather-related error.

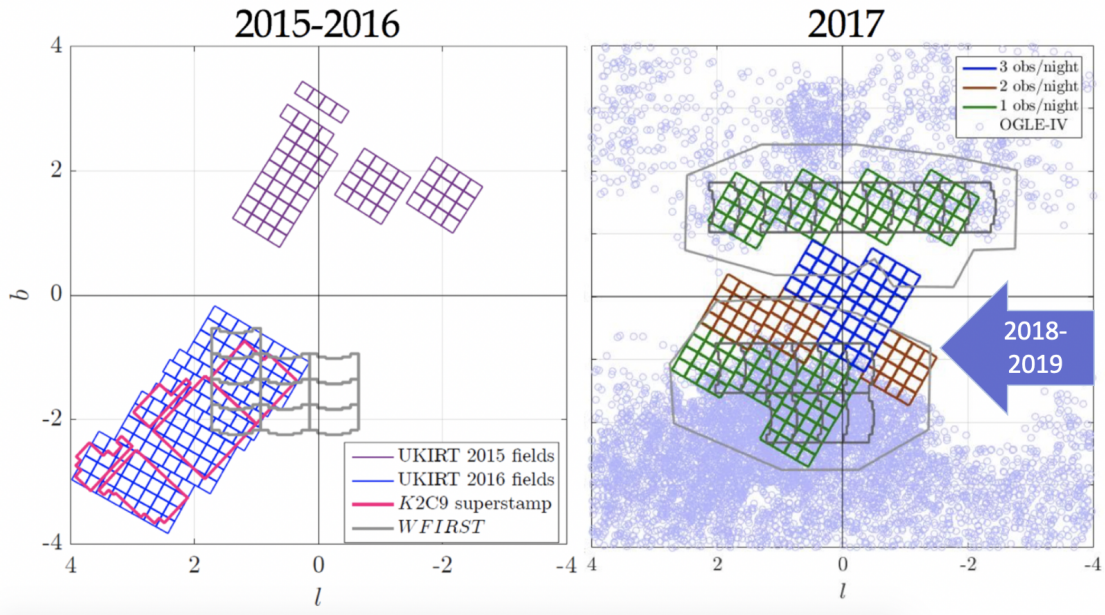

Figure 5.1: UKIRT microlensing survey 2015-2019 observational fields. The plot on the left shows UKIRT's 2015-2016 observations. Each 2015 field had a cadence of 5 epochs per night and 2016 fields were observed 2-3 times per night. Red outlines show the K2 Campaign 9 fields which were observed concurrently in 2016. The right plot depicts the survey fields in 2017. 2018 and 2019 fields are similar to 2017, but eliminate those four fields located north of the Bulge. Green field were observed at a cadence of one observation per night, red fields were observed twice per night, and blue fields (fields closest to the Galactic center) were observed three times per night. Solid grey lines on both plots signify proposed WFIRST fields, and blue semi-transparent circles signify OGLE IV observations [28]. [39]

5.2.2 UKIRT Microlensing Event Simulations and Recovery with MISIRY

5.2.2.1 MISIRY Pipeline Overview

In this section, we describe the custom data processing pipeline that we have developed for the purpose of analyzing real UKIRT survey images and extracting light curves of sources, and for injecting simulated light curves into the images for the purposes of testing our survey sensitivity and completeness. Figure 5.2 presents a visual summary of MISIRY, the Microlensing Infrared Simulated Injection and RecoverY pipeline. With MISIRY, the injected light curves are broken into three distinct categories: flat stars, point-source-point-lens (PSPL) microlensing stars, and binary-lens (exoplanet) stars. We focus primarily on flat and PSPL stellar injections due to the UKIRT Microlensing Survey's limited cadence; although we can and have detected planets, we are not optimized for such observations. Therefore, we chose to instead focus on generating a high quality and flexible injection pipeline, with eventual goal of understanding our survey's microlensing detection efficiency as a path to defining the microlensing event rate. Although we have not yet determined a definitive answer to the previous two questions, the MISIRY pipeline will be able to provide answers with additional computation and analysis time. MISIRY is a data-intensive pipeline, and is therefore designed to run on supercomputer clusters as opposed to individual machines. We describe MISIRY in detail in the following subsections.

5.2.2.2 Common Parameters

We begin our simulations by first defining a set of core variables that carry on throughout. These variables include the name of the run, field of observation, CCD number (1-4), year (2015-2019), band (H or K), number of non-variable (flat) stars, number of PSPL microlensing stars, number of binary lens stars, and the magnitude distribution from which you should inject mock stars. We then create a series of bash scripts that break our mock star injection pipeline into six steps that are then run on the NASA Jet Propulsion Laboratory supercomputers.

We define a data structure for each given simulation, which in turn affects how MISIRY runs

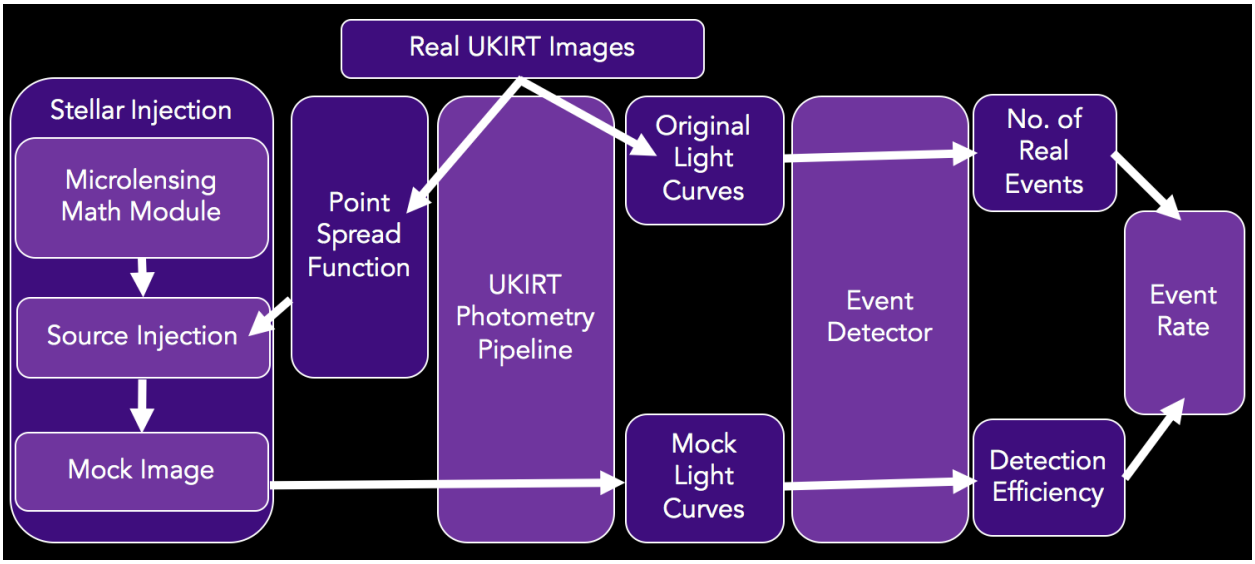

Figure 5.2: MISIRY pipeline schematic. The pipeline is structured such that both real and mock images are processed via the same photometry extraction processes in order to determine the number of real events and the microlensing detection efficiency as an avenue to determining the microlensing event rate.

throughout the injection and recovery process. The data structure contains the common parameters described above, as well as values specific to the UKIRT Microlensing Survey and our observations. The purpose of holding changing variables in one specific class is to make MISIRY as flexible as possible. In theory, MISIRY should be able to inject any type of star into any type of image from any telescope with minimal alterations to the pipeline base code. In the case of the microlensing survey, we adjust the data structure's values to UKIRT's observational parameters and our survey structure, and create image-level injected star simulations that contain flat and PSPL stars.

5.2.2.3 Point Spread Function Generation

After making variable selections, the first stage of our simulation runs each real UKIRT image through the initial MISIRY pipeline. Source detection (i.e. the isolation and detection of real stars) is accomplished using SourceExtractor [6]. These sources are then used to create a model point spread function (PSF) for each individual image using PSFExtractor [5]. The PSFs generated are softened exponential Moffat PSFs with 75 x 75 pixel PSF image sizes at 0.2 pixel oversampling for each epoch and CCD. There is an approximately 2% variation in the flux across each CCD due to variations in the PSF. Each of these PSF generation parameters has been optimized for the UKIRT Microlensing Survey, but may also be altered in the data structure if necessary.

5.2.2.4 Real Source Light Curve Generation

Step two begins by determining the normalization factors for each of our model fits. Each PSF fits file as a function of epoch is summed, and the total value is recorded per pixel as a normalization factor N. We then take the normalization factors and use them to create a global zero point Z_{global} as a function of CCD using the equation

$$Z_{global} = median(2.5\log_{10}(N(t))) \; . \tag{5.1}$$

The pipeline then moves on to detect and generate light curves for each source. First we utilize SourceExtractor to single out each individual light source in an image (parameters specific to our source detection are defined in the data structure). Next we convert the source positions x- and y- coordinates into right ascension (RA) and declination (Dec) sky coordinates from the first epoch of our simulation. We then query the VizieR database of astronomical catalogues [30] for SourceExtractor-detected bright stars with absolute magnitudes between 12 and 14 that contain matching coordinates from the Two Micron All Sky Survey (2MASS) catalog [41]. [1] This enables us to then calibrate the magnitudes of each source to a reliable value. We repeat this process for each epoch in our simulation where any newly-detected sources are appended as the iterations proceed. Once source position and magnitude matching is complete, MISIRY creates separate master files for magnitude, magnitude error, x-position, y-position, right ascension, declination, seeing, and background for each detected source. If any of the values in these master files are equivalent to zero (akin to a non-detection), we convert the zeros into nans.

The final portion of light curve generation calculates a variety of statistics for each light curve. We first find the nearest star to the source and then calculate the zero point offset by comparing the 2MASS calibration match to the raw magnitude of our detection. The final magnitude is subsequently adjusted by the correct zero point offset per epoch, and the number of data points per source light curve is calculated. We then calculate the root-mean square and median absolute deviation of each light curve, and match each source to the right ascension and declination. Each of these values are added to distinct text files that are used to generate light curves and their associated statistics in later data analysis.

5.2.2.5 Injection of Simulated Light Curves

Now that we have a template PSFs for each epoch and CCD, we can inject mock stars at the image level. The first step in the injection process is to create the files that contain all the necessary parameters that define the types of injected stars. We begin by loading UKIRT-specific files that

[1] Note that we only match stars from our brightest sources due to the fact that the UKIRT Microlensing Survey looks at fainter stars than 2MASS.

contain information on the year, field, CCD, and spatial edges of each UKIRT observation. These files dictate where and when we can place mock injections, and are necessary for creating all types of mock stars (i.e., flat, PSPL, or binary lens). These master files are used to generate a grid of 10,000 possible injection sites in RA-Dec space per CCD. Then we take a random sampling of the positions in this grid equivalent to the number of stars that the user has selected for injection. Since they are non-varying, flat stars need only an initial magnitude and position at this stage to be injected. In addition to initial magnitude and position, each PSPL injection is assigned a value of t_E, t_0, and u_0.[2]

Now that we have determined a set of microlensing parameters, we can calculate how the microlensing signal evolves over time. We combine it the original magnitude M with magnification A (see Introduction), to determine the magnitude of the source at the following epoch

$$M(t) = M(t-1) - 2.5\log(A)\,. \tag{5.2}$$

We must convert this magnitude into flux units F in order to inject the star at the image level. This is accomplished via

$$F(t) = N(t) \times 10^{-0.4M(t)-24-Z(t)+Z_{global}}\,, \tag{5.3}$$

where $Z(t)$ is the calculated zero point of the epoch, and 24 is a default zero point factor calculated for the UKIRT Microlensing survey. The magnification, magnitude, and flux are all calculated across the axes of epoch for each star.

Now that we have a flux, magnification, injection number, epoch, right ascension, and declination for each star to be injected, MISIRY is able to inject stars. MISIRY overlays mock stars with the specified parameters over the top of the original observational image and saves this blended

[2]MISIRY is capable of injecting a binary lens signal, which must also include values for the projected separation s, mass ratio q, light bending angle α, and finite source effects ρ. We utilize MulensModel [34] and VBBL [10], which are public microlensing fitting routines, in order to determine the magnification caused by the third body introduced into binary lens system.

mock + real image as a new file. This process is repeated as a function of epoch and CCD for a given simulation.

5.2.2.6 Extraction of Injected Light Curves

In order to make sure our photometry pipeline is self-consistent, we perform our injected light curve extraction on the newly generated images via the same process as our real images. Mock images are processed by SourceExtractor and PSFExtractor, with the only difference being that the image size of the PSF model is reduced to the standard 25 x 25 pixels with no oversampling. Injected sources are searched for on the image level with a maximum of 0.6" radius from the injected position. The end result of repeating these processes is the generation of both mock and real recovered light curves and their associated errors, positions, background, seeing, and zero points. These light curves are the final product of the MISIRY pipeline.

5.2.3 Example Light Curves

Here we show a few examples of injected and extracted MISIRY light curves. Figure 5.3 displays a flat star injection to highlight the average level of noise in any given light curve. Figure 5.4 shows an injected PSPL light curve and Figure 5.5displays its resultant fit and residuals. As can be clearly seen by the fit, lack of cadence coverage at the peak of the event is a major driver of fitting errors.

5.2.4 Assessment of Photometric Outputs

The goal of looking at the median absolute deviation of our injected stars vs. the real stars in an image is to test just how real our mock stars appear. In Figure 5.6, we examine the median absolute deviation as a function of magnitude for CCD 1 of 2015, 2016, and 2017 injections of flat stars. We only plot stars that are found by MISIRY in at least 10% of the light curves for a given year of observation. Since the injected stars (blue) line up well with the real stars (black) in the median absolute deviation space, we know that to MISIRY, our injected stars are indistinguishable from real stars.

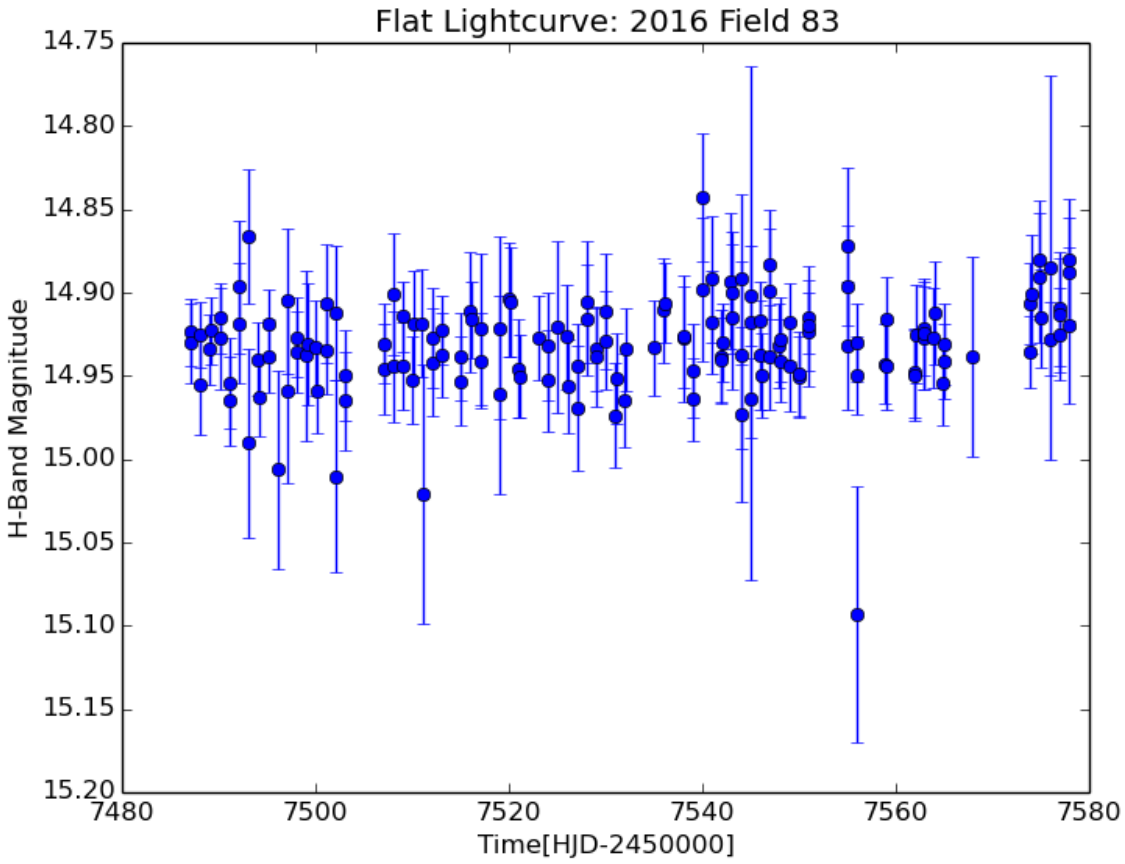

Figure 5.3: MISIRY-injected flat star light curve. This light curve shows the average level of noise for a star of this magnitude for the UKIRT Microlensing Survey.

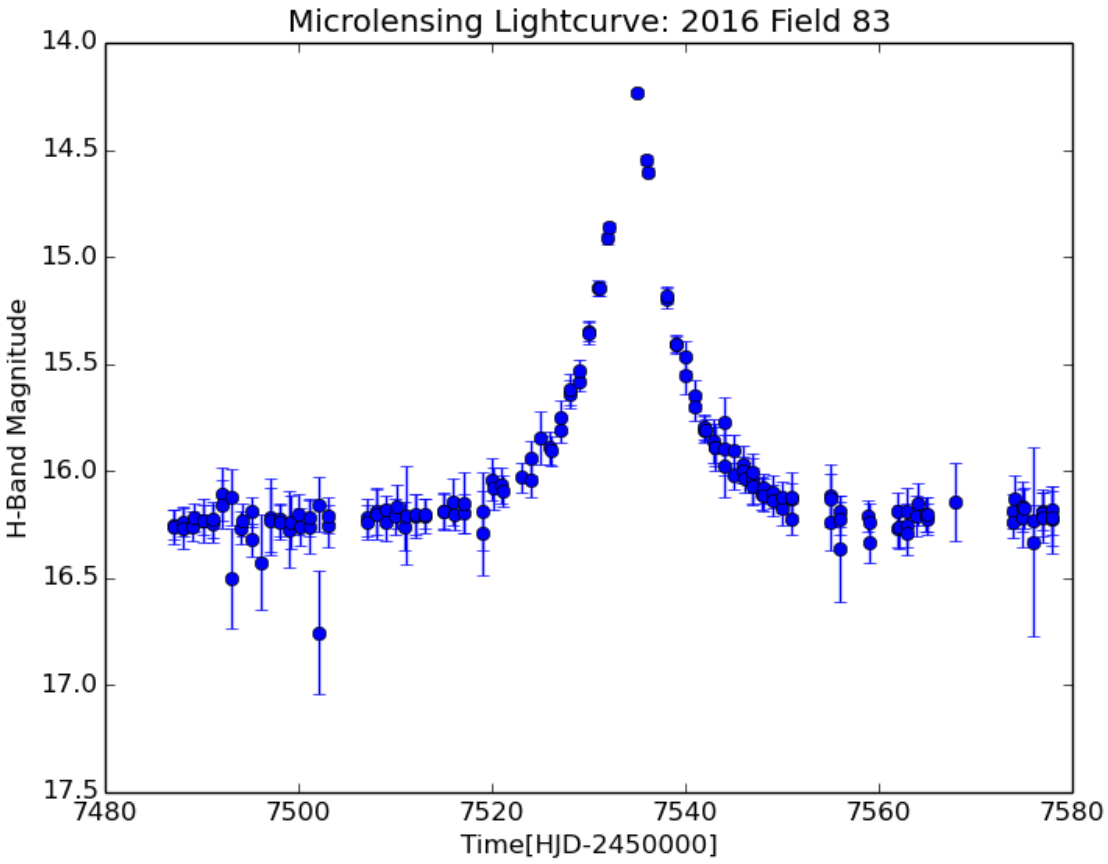

Figure 5.4: MISIRY-injected microlensing light curves and resultant fit. this star was injected with $t_E = 10.02374467$, $t_0 = 7542.03793654$, *and* $u_0 = 0.38703467$.

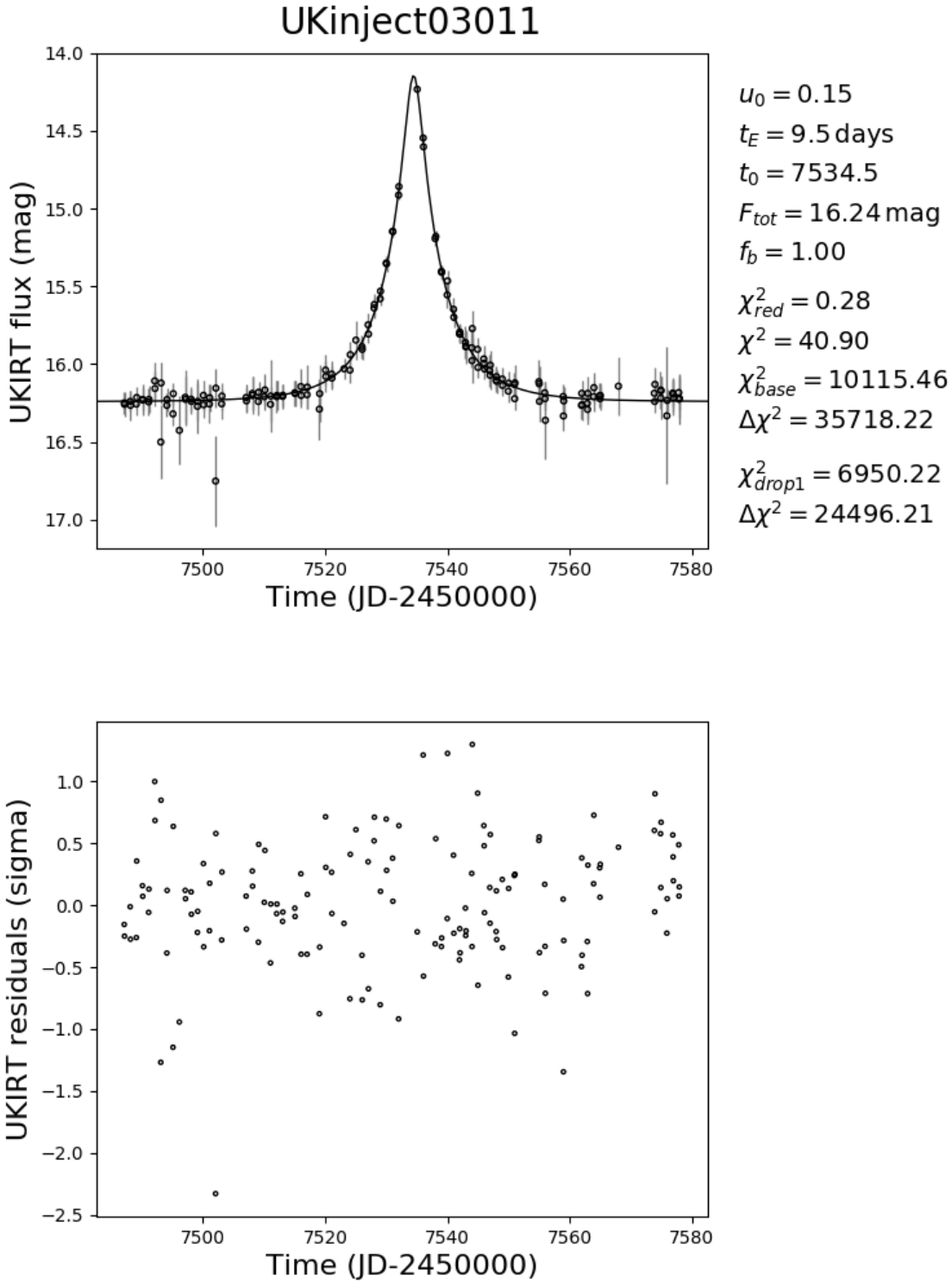

Figure 5.5: Resultant MCMC fit and residuals of the injected light curve in Figure 5.4. Errors can largely be attributed to lack of cadence coverage at the peak magnification.

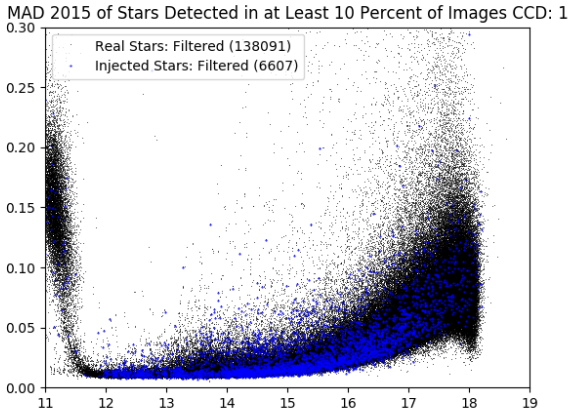

(a) 2015

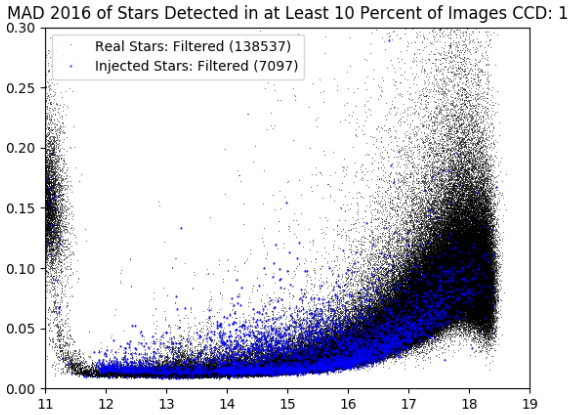

(b) 2016

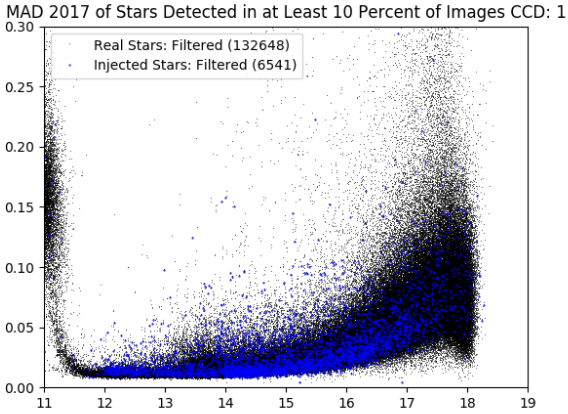

(c) 2017

Figure 5.6: Median absolute deviation of injected stars recovered in 10% of epochs per year.

Year	Field	Cadence/night	Band
2015	13	5x	H
2016	12	2x	H
2016	43	2x	H
2016	83	2x	H
2017	n2_3	1x	H
2017	s3_2	1x	H
2017	s1_1	2x	K
2017	c4_4	3x	K

Table 5.1: Completeness fields.

5.3 Results and Discussion

5.3.1 Completeness Study

In order to measure completeness, we follow the example steps laid out by Mróz et al. [28]. As shown in Table 5.1, our completeness analysis covers a variety of take exemplar fields from a variety of cadences and from each year to inject flat stars.

Each CCD is injected with 4000 stars with magnitudes drawn from binned uniform distributions, where 500 stars are injected $12^{th} - 14^{th}$ magnitude, 1500 stars from $14^{th} - 16^{th}$ magnitude, and 2000 stars from $16^{th} - 18^{th}$ magnitude. These simulations are run through the totality of the MISIRY pipeline, yielding recovered light curves.

Deciding which injected stars are considered to be recovered is not a trivial process. After considerable deliberation, it was determined that recoverability of a flat star would be defined utilizing the median absolute deviation. First, injected stars are broken into magnitude bins from $12^{th} - 18^{th}$ magnitudes in single magnitude increments. Then, we take the median of the recovered magnitudes of each star's light curve and subtract the star's injected magnitude. We then calculate the median and the median absolute deviations of all stars that fall within a given bin. If the difference between the recovered magnitude of the star and its injected magnitude falls within ± 3 median absolute deviations of the median of the brightest bin, the injected star is considered to be recovered. This process is then repeated bin-wise for all injected stars. Figure 5.7 shows what this cut looks like for each of our magnitude bins for CCD 1 of each of our completeness simulations.

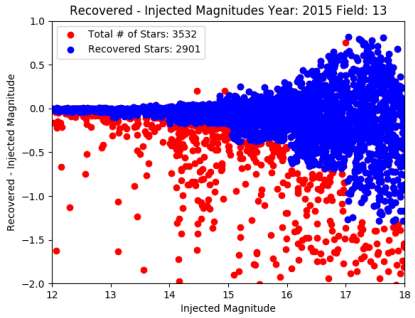

(a) 2015 Field 13

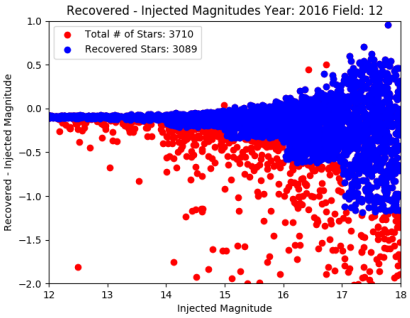

(b) 2016 Field 12

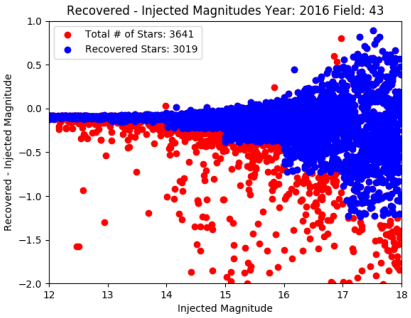

(c) 2016 Field 43

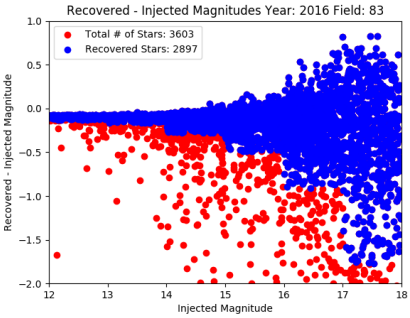

(d) 2016 Field 83

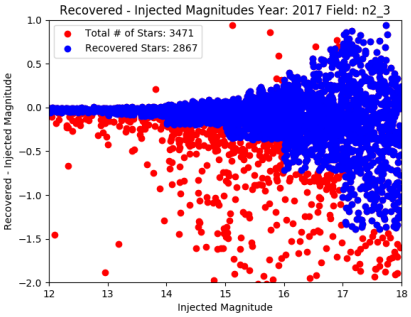

(e) 2017 Field n2_3

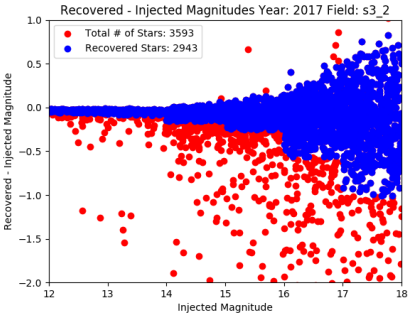

(f) 2017 Field s3_2

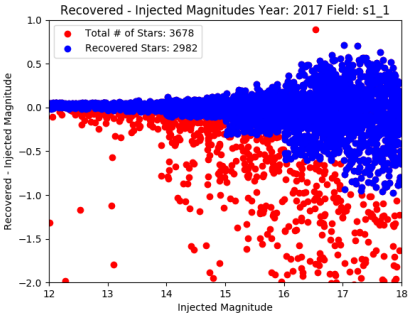

(g) 2017 Field s1_1

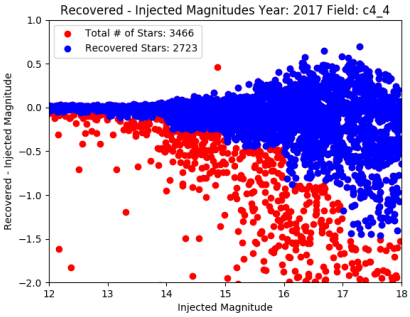

(h) 2017 Field c4_4

Figure 5.7: Binned median absolute deviation magnitude cuts. Blue points are recovered stars, red points are not considered to be recovered.

Now that we know which stars have been recovered, we can determine the completeness of our UKIRT Microlensing Survey as a function of magnitude. The resultant values vary depending on each of the input parameters of a given simulation. The final completeness plots for each one of our simulated fields is shown in Figure 5.8.

5.3.2 Luminosity Function

Once the completeness as a function of magnitude has been determined, we can return to our original survey to determine the luminosity function of our stars and correct for the completeness. The derived luminosity functions are shown in Figure 5.9. Note that only stars within the range $12^{th} - 18^{th}$ magnitude are included in this analysis since that is the range for which we have derived completeness factors. A discussion on the extrapolation of luminosity functions may be found in Mróz et al. [28].

5.3.3 Real Microlensing Events

The uppermost track of our NIR detection efficiency pipeline is concerned with the detection of actual microlensing events occurring within all years of UKIRT observations. Once we have used our UKIRT photometry pipeline to process and extract the sources from all of our real images, we will be able to build light curves for all sources exhibiting a microlensing signal over time. These light curves will then be processed via the machine learning event finder in order to determine the total number of real microlensing events observed by UKIRT. Anomalous events (i.e. events exhibiting evidence of a planetary companion to the lens) in particular will be published as they are detected, such as the five events described in Shvartzvald et al. [39]. We recently detected and published our first UKIRT-only observations of a microlensing event [40]. The light curve of this microlensing exoplanet detection is reproduced in Figure 5.10.

5.3.4 Machine Learning Event Detector

Whether or not an injected microlensing event is recovered depends on many factors such as the baseline brightness of the source star, how much it is amplified during the event, the timing of

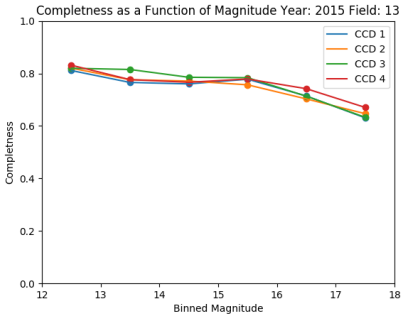

(a) 2015 Field 13

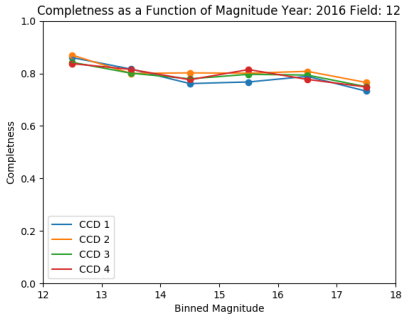

(b) 2016 Field 12

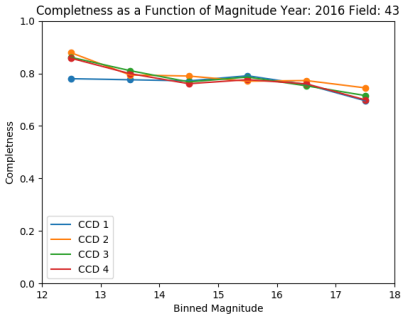

(c) 2016 Field 43

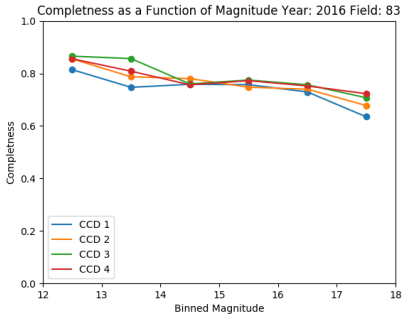

(d) 2016 Field 83

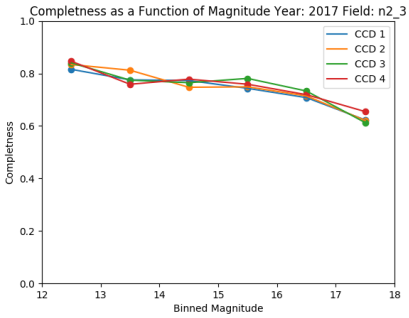

(e) 2017 Field n2_3

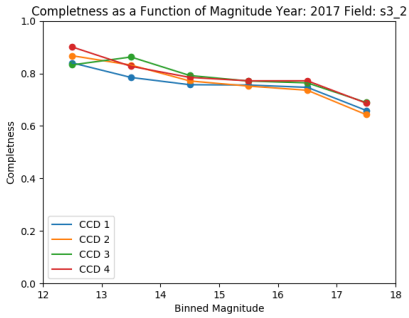

(f) 2017 Field s3_2

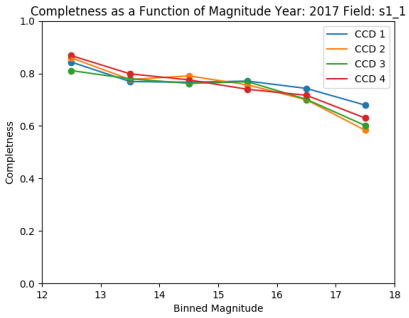

(g) 2017 Field s1_1

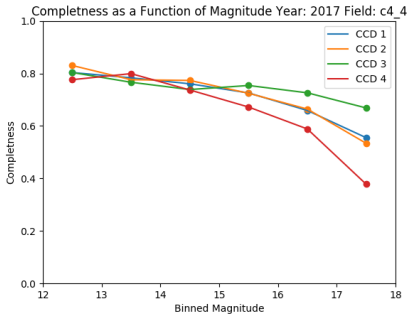

(h) 2017 Field c4_4

Figure 5.8: Completeness as a function of median magnitude for each year-field combinations of simulations. This general shape is expected, with recovery of almost all bright stars, with completeness dropping as a function of magnitude.

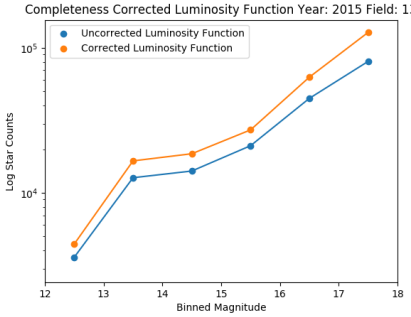

(a) 2015 Field 13

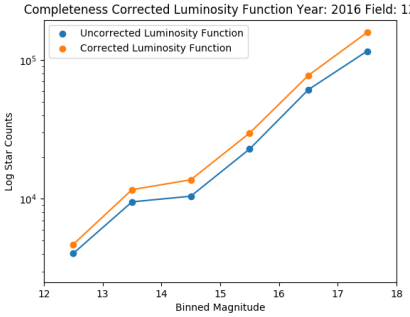

(b) 2016 Field 12

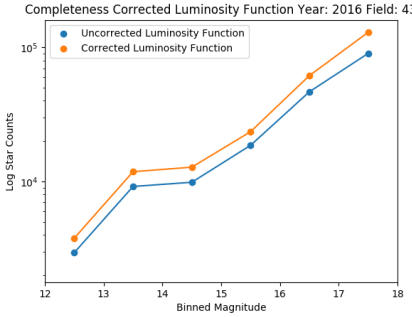

(c) 2016 Field 43

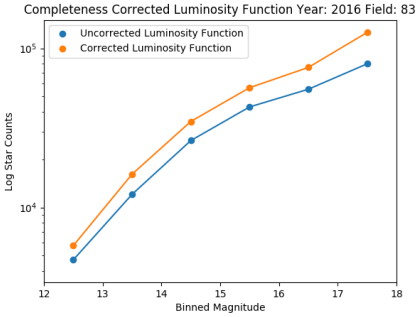

(d) 2016 Field 83

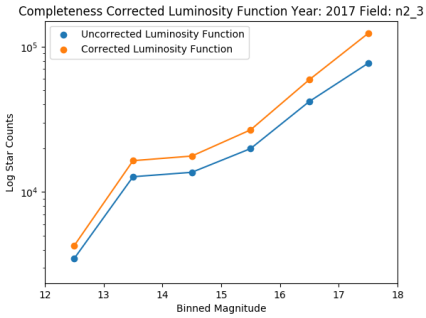

(e) 2017 Field n2_3

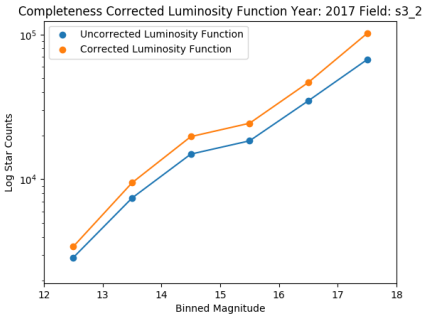

(f) 2017 Field s3_2

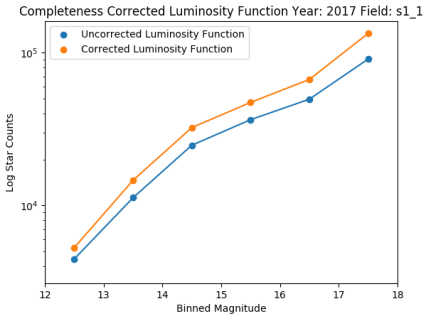

(g) 2017 Field s1_1

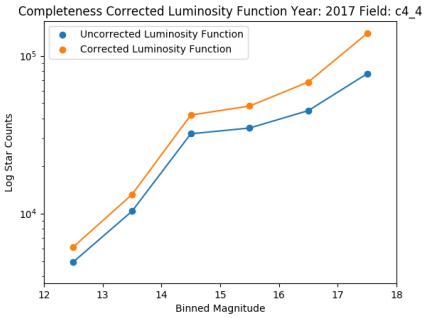

(h) 2017 Field c4_4

Figure 5.9: Uncorrected and corrected luminosity functions for CCD 1 for each completeness field.

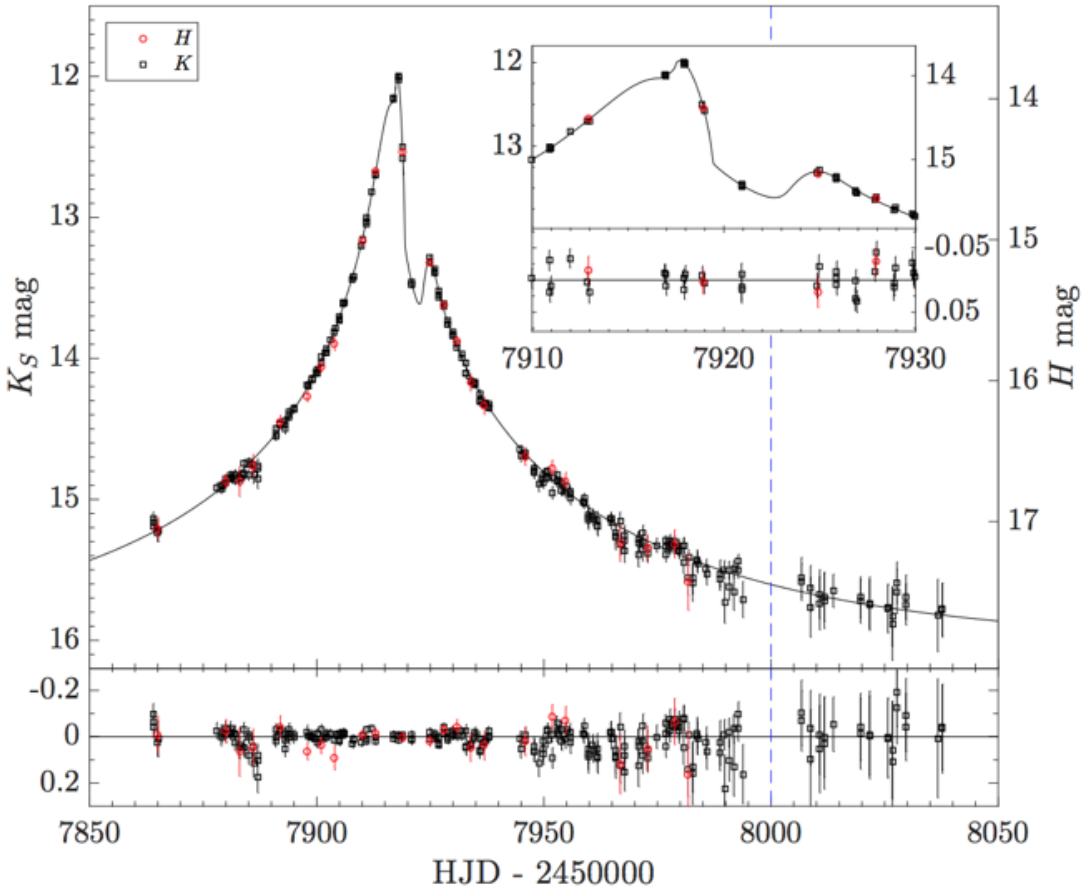

Figure 5.10: The first UKIRT-only microlensing exoplanet detection from Shvartzvald et al. [40]. This planet is embedded so heavily in the dust at the Galactic center that only UKIRT with its unique NIR sensitivity was able to make the detection.

the event relative to the observing window, and whether it is blended with a nearby brighter star. To systematically decide whether a given event is detected, we use an automated machine-learning scheme to classify all of the simulated light curves. For consistency, this event detection process is identical to the one used for the real light curves [12]. This work is currently still in progress, but all simulations covering a wide variety of PSPL stellar injections have been completed. The resultant light curves will be fed into the machine learning event detector, and will subsequently reveal the microlensing parameters to which we are most sensitive. We choose the following parameters for our microlensing injections:

parameter	range	spacing	# of values
F_s	12 – 19 mag	linear	binned values described above
t_E	2 – 100 days	log	21
t_0	(seasonal) ($\pm$30 days)	linear	random sampling
u_0	0.01 – 1.1	log	10
ρ	0.001	constant	1

Since we are not yet able to fully characterize our light curves with a full MCMC analysis, we instead use a grid fit method pioneered by Andy Gould. This provides a fast characterization of events, labelling all that have a χ^2 as detected microlensing. The most interesting parameter space of event detection that we wanted to explore was the number of injections as a function of t_E. Preliminary results using the above simulations and the grid fit event classifier are shown in 5.11. These detections are corrected as a function of u_0 and our derived luminosity function.

5.3.5 NIR Microlensing Event Rate

Combining the data products from both the NIR microlensing detection efficiency as well as a total number of real microlensing events helps to determine a total NIR event rate at low Galactic latitudes. Previous surveys that have attempted to determine microlensing event rates have been forced to avoid observing the Galactic center due to the obscuring presence of dust [44]. UKIRT's unique ability to peer through this dust using the NIR H and K bands will allow us to be the first

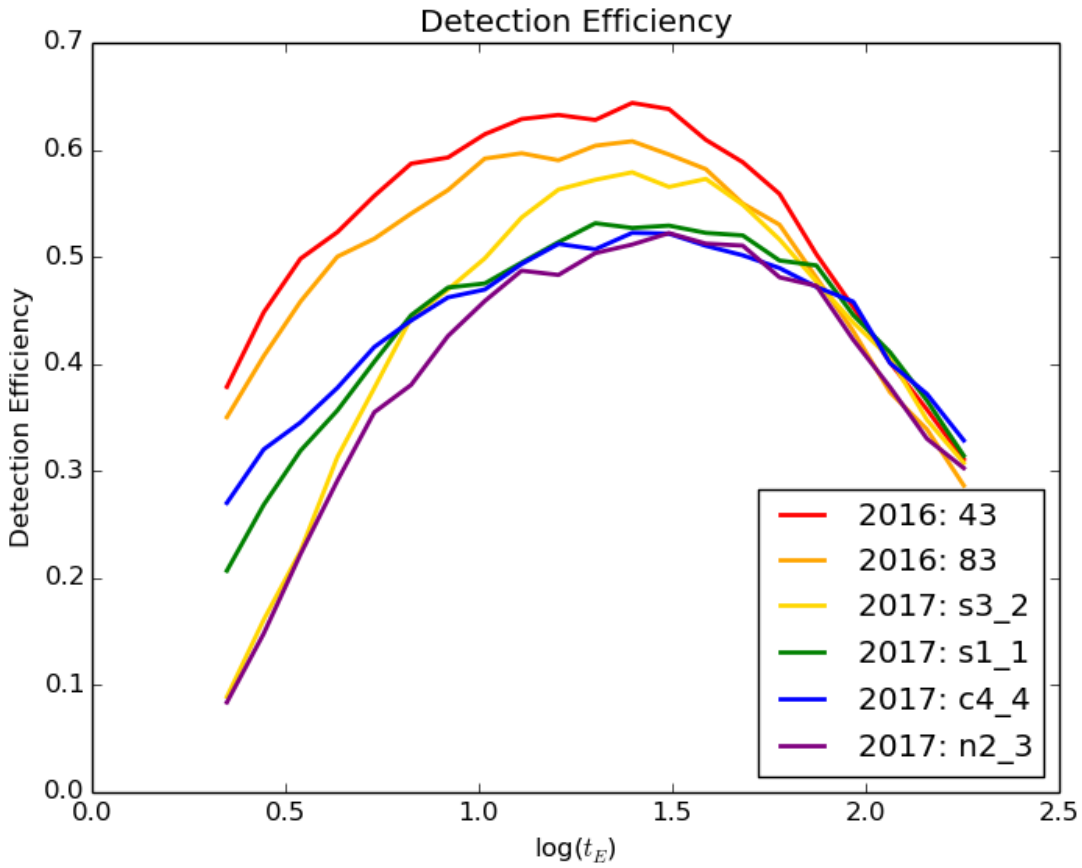

Figure 5.11: Number of microlensing event detections as a function of t_E for each field. Note that fields 2015_23 and 2016_12 have been removed from this analysis due to incomplete simulations.

to determine the NIR microlensing event rate per square degree to a precision of $\sim$10%. With this data we will be well-poised to inform on WFIRST observational field and design specifications. This is the ultimate end goal of the UKIRT Microlensing Survey, proving that this project is an example of what we can do today in preparation for tomorrow.

Chapter 6

Conclusions

Astronomy in the twenty first century is a rapidly growing field, evolving hand in hand with new technologies. The CCD has enabled the large-scale study of the changing night sky, allowing astronomers to create light curves for thousands of objects at once and monitor their changes in real time. However, with great new technology comes great new challenges in data processing. The Vera C. Rubin Observatory will take nearly 20 TB of data per night, necessitating new ways to rapidly identify transient objects. Similarly, the massive data flow UKIRT Microlensing Survey is an example of one of the challenges that come with rapidly and accurately classifying large numbers of microlensing events. Our work with VRO simulations and UKIRT has been completed with the goal of creating software architectures and beginning to answer science questions that can be applied to next generation surveys. When the WFIRST microlensing survey begins, the problem of microlensing characterization will face a dramatic increase in scale.

Another question involving such large-scale next generation telescopes is what exactly will they be able to detect. Astronomers will not know for sure what a telescope will see until it achieves first light, but we can make predictions based on instrument design and observational field locations. Generating predictions is a far from trivial process, and has been the goal of both parts of this thesis. We were able to use the operations simulation of VRO to reveal that this next-generation telescope can indeed discover new exoplanets. Moreover, we calculated which types of exoplanets VRO will be best poised to detect considering its suboptimal transiting exoplanet cadence, as well as how quickly these detections will occur. These predictions were the result of extensive simulations using light curve level exoplanet injection and recovery codes. Our work with VRO represents the narrow line between theoretical (simulation-based) and observational astronomy, and highlights a need for accurate communication between the two in order to prepare for the future of astronomy.

In a similar track, our UKIRT Microlensing survey blended real and simulated observations

in order to characterize the potential of our survey. Our goal was to determine the real number of microlensing events, build a software photometry pipeline, derive our survey's completeness and luminosity functions, calculate our microlensing detection efficiency, and combine all of these values into a calculation of the microlensing event rate near the Galactic center. Although there is still some work to do in refining the detection efficiency and calculating the event rate, we have accomplished a great deal for a small team working on a large survey. Our derived science is sound, and the MISIRY pipeline is specialized but flexible enough to be adapted to future surveys of the Galactic Bulge or other crowded stellar density fields.

The results of this thesis are only scratching the surface of the multitudinous science that can be done in the new era of the lightcurve. I, for one, am looking forward to seeing what comes next.

BIBLIOGRAPHY

[1] Abbott, B. P., Abbott, R., Abbott, T. D., Abernathy, M. R., Acernese, F., Ackley, K., Adams, C., Adams, T., Addesso, P., Adhikari, R. X., Adya, V. B., Affeldt, C., Agathos, M., Agatsuma, K., Aggarwal, N., Aguiar, O. D., Aiello, L., Ain, A., Ajith, P., Allen, B., Allocca, A., Altin, P. A., Anderson, S. B., Anderson, W. G., Arai, K., Arain, M. A., Araya, M. C., Arceneaux, C. C., Areeda, J. S., Arnaud, N., Arun, K. G., Ascenzi, S., Ashton, G., Ast, M., Aston, S. M., Astone, P., Aufmuth, P., Aulbert, C., Babak, S., Bacon, P., Bader, M. K. M., Baker, P. T., Baldaccini, F., Ballardin, G., Ballmer, S. W., Barayoga, J. C., Barclay, S. E., Barish, B. C., Barker, D., Barone, F., Barr, B., Barsotti, L., Barsuglia, M., Barta, D., Bartlett, J., Barton, M. A., Bartos, I., Bassiri, R., Basti, A., Batch, J. C., Baune, C., Bavigadda, V., Bazzan, M., Behnke, B., Bejger, M., Belczynski, C., Bell, A. S., Bell, C. J., Berger, B. K., Bergman, J., Bergmann, G., Berry, C. P. L., Bersanetti, D., Bertolini, A., Betzwieser, J., Bhagwat, S., Bhandare, R., Bilenko, I. A., Billingsley, G., Birch, J., Birney, R., Birnholtz, O., Biscans, S., Bisht, A., Bitossi, M., Biwer, C., Bizouard, M. A., Blackburn, J. K., Blair, C. D., Blair, D. G., Blair, R. M., Bloemen, S., Bock, O., Bodiya, T. P., Boer, M., Bogaert, G., Bogan, C., Bohe, A., Bojtos, P., Bond, C., Bondu, F., Bonnand, R., Boom, B. A., Bork, R., Boschi, V., Bose, S., Bouffanais, Y., Bozzi, A., Bradaschia, C., Brady, P. R., Braginsky, V. B., Branchesi, M., Brau, J. E., Briant, T., Brillet, A., Brinkmann, M., Brisson, V., Brockill, P., Brooks, A. F., Brown, D. A., Brown, D. D., Brown, N. M., Buchanan, C. C., Buikema, A., Bulik, T., Bulten, H. J., Buonanno, A., Buskulic, D., Buy, C., Byer, R. L., Cabero, M., Cadonati, L., Cagnoli, G., Cahillane, C., Bustillo, J. C., Callister, T., Calloni, E., Camp, J. B., Cannon, K. C., Cao, J., Capano, C. D., Capocasa, E., Carbognani, F., Caride, S., Diaz, J. C., Casentini, C., Caudill, S., Cavaglià, M., Cavalier, F., Cavalieri, R., Cella, G., Cepeda, C. B., Baiardi, L. C., Cerretani, G., Cesarini, E., Chakraborty, R., Chalermsongsak, T., Chamberlin, S. J., Chan, M., Chao, S., Charlton, P., Chassande-Mottin, E., Chen, H. Y., Chen, Y., Cheng, C., Chincarini, A., Chiummo, A., Cho, H. S., Cho, M., Chow, J. H., Christensen, N., Chu, Q., Chua, S., Chung, S., Ciani, G., Clara, F., Clark, J. A., Cleva, F.,

Coccia, E., Cohadon, P.-F., Colla, A., Collette, C. G., Cominsky, L., Constancio, M., Conte, A., Conti, L., Cook, D., Corbitt, T. R., Cornish, N., Corsi, A., Cortese, S., Costa, C. A., Coughlin, M. W., Coughlin, S. B., Coulon, J.-P., Countryman, S. T., Couvares, P., Cowan, E. E., Coward, D. M., Cowart, M. J., Coyne, D. C., Coyne, R., Craig, K., Creighton, J. D. E., Creighton, T. D., Cripe, J., Crowder, S. G., Cruise, A. M., Cumming, A., Cunningham, L., Cuoco, E., Canton, T. D., Danilishin, S. L., D'Antonio, S., Danzmann, K., Darman, N. S., Da Silva Costa, C. F., Dattilo, V., Dave, I., Daveloza, H. P., Davier, M., Davies, G. S., Daw, E. J., Day, R., De, S., DeBra, D., Debreczeni, G., Degallaix, J., De Laurentis, M., Deléglise, S., Del Pozzo, W., Denker, T., Dent, T., Dereli, H., Dergachev, V., DeRosa, R. T., De Rosa, R., DeSalvo, R., Dhurandhar, S., Díaz, M. C., Di Fiore, L., Di Giovanni, M., Di Lieto, A., Di Pace, S., Di Palma, I., Di Virgilio, A., Dojcinoski, G., Dolique, V., Donovan, F., Dooley, K. L., Doravari, S., Douglas, R., Downes, T. P., Drago, M., Drever, R. W. P., Driggers, J. C., Du, Z., Ducrot, M., Dwyer, S. E., Edo, T. B., Edwards, M. C., Effler, A., Eggenstein, H.-B., Ehrens, P., Eichholz, J., Eikenberry, S. S., Engels, W., Essick, R. C., Etzel, T., Evans, M., Evans, T. M., Everett, R., Factourovich, M., Fafone, V., Fair, H., Fairhurst, S., Fan, X., Fang, Q., Farinon, S., Farr, B., Farr, W. M., Favata, M., Fays, M., Fehrmann, H., Fejer, M. M., Feldbaum, D., Ferrante, I., Ferreira, E. C., Ferrini, F., Fidecaro, F., Finn, L. S., Fiori, I., Fiorucci, D., Fisher, R. P., Flaminio, R., Fletcher, M., Fong, H., Fournier, J.-D., Franco, S., Frasca, S., Frasconi, F., Frede, M., Frei, Z., Freise, A., Frey, R., Frey, V., Fricke, T. T., Fritschel, P., Frolov, V. V., Fulda, P., Fyffe, M., Gabbard, H. A. G., Gair, J. R., Gammaitoni, L., Gaonkar, S. G., Garufi, F., Gatto, A., Gaur, G., Gehrels, N., Gemme, G., Gendre, B., Genin, E., Gennai, A., George, J., Gergely, L., Germain, V., Ghosh, A., Ghosh, A., Ghosh, S., Giaime, J. A., Giardina, K. D., Giazotto, A., Gill, K., Glaefke, A., Gleason, J. R., Goetz, E., Goetz, R., Gondan, L., González, G., Castro, J. M. G., Gopakumar, A., Gordon, N. A., Gorodetsky, M. L., Gossan, S. E., Gosselin, M., Gouaty, R., Graef, C., Graff, P. B., Granata, M., Grant, A., Gras, S., Gray, C., Greco, G., Green, A. C., Greenhalgh, R. J. S., Groot, P., Grote, H., Grunewald, S., Guidi, G. M., Guo, X., Gupta, A., Gupta, M. K., Gushwa, K. E., Gustafson, E. K., Gustafson, R., Hacker, J. J., Hall, B. R.,

Hall, E. D., Hammond, G., Haney, M., Hanke, M. M., Hanks, J., Hanna, C., Hannam, M. D., Hanson, J., Hardwick, T., Harms, J., Harry, G. M., Harry, I. W., Hart, M. J., Hartman, M. T., Haster, C.-J., Haughian, K., Healy, J., Heefner, J., Heidmann, A., Heintze, M. C., Heinzel, G., Heitmann, H., Hello, P., Hemming, G., Hendry, M., Heng, I. S., Hennig, J., Heptonstall, A. W., Heurs, M., Hild, S., Hoak, D., Hodge, K. A., Hofman, D., Hollitt, S. E., Holt, K., Holz, D. E., Hopkins, P., Hosken, D. J., Hough, J., Houston, E. A., Howell, E. J., Hu, Y. M., Huang, S., Huerta, E. A., Huet, D., Hughey, B., Husa, S., Huttner, S. H., Huynh-Dinh, T., Idrisy, A., Indik, N., Ingram, D. R., Inta, R., Isa, H. N., Isac, J.-M., Isi, M., Islas, G., Isogai, T., Iyer, B. R., Izumi, K., Jacobson, M. B., Jacqmin, T., Jang, H., Jani, K., Jaranowski, P., Jawahar, S., Jiménez-Forteza, F., Johnson, W. W., Johnson-McDaniel, N. K., Jones, D. I., Jones, R., Jonker, R. J. G., Ju, L., Haris, K., Kalaghatgi, C. V., Kalogera, V., Kandhasamy, S., Kang, G., Kanner, J. B., Karki, S., Kasprzack, M., Katsavounidis, E., Katzman, W., Kaufer, S., Kaur, T., Kawabe, K., Kawazoe, F., Kéfélian, F., Kehl, M. S., Keitel, D., Kelley, D. B., Kells, W., Kennedy, R., Keppel, D. G., Key, J. S., Khalaidovski, A., Khalili, F. Y., Khan, I., Khan, S., Khan, Z., Khazanov, E. A., Kijbunchoo, N., Kim, C., Kim, J., Kim, K., Kim, N.-G., Kim, N., Kim, Y.-M., King, E. J., King, P. J., Kinzel, D. L., Kissel, J. S., Kleybolte, L., Klimenko, S., Koehlenbeck, S. M., Kokeyama, K., Koley, S., Kondrashov, V., Kontos, A., Koranda, S., Korobko, M., Korth, W. Z., Kowalska, I., Kozak, D. B., Kringel, V., Krishnan, B., Królak, A., Krueger, C., Kuehn, G., Kumar, P., Kumar, R., Kuo, L., Kutynia, A., Kwee, P., Lackey, B. D., Landry, M., Lange, J., Lantz, B., Lasky, P. D., Lazzarini, A., Lazzaro, C., Leaci, P., Leavey, S., Lebigot, E. O., Lee, C. H., Lee, H. K., Lee, H. M., Lee, K., Lenon, A., Leonardi, M., Leong, J. R., Leroy, N., Letendre, N., Levin, Y., Levine, B. M., Li, T. G. F., Libson, A., Littenberg, T. B., Lockerbie, N. A., Logue, J., Lombardi, A. L., London, L. T., Lord, J. E., Lorenzini, M., Loriette, V., Lormand, M., Losurdo, G., Lough, J. D., Lousto, C. O., Lovelace, G., Lück, H., Lundgren, A. P., Luo, J., Lynch, R., Ma, Y., MacDonald, T., Machenschalk, B., MacInnis, M., Macleod, D. M., Magaña Sandoval, F., Magee, R. M., Mageswaran, M., Majorana, E., Maksimovic, I., Malvezzi, V., Man, N., Mandel, I., Mandic, V., Mangano, V., Mansell, G. L.,

Manske, M., Mantovani, M., Marchesoni, F., Marion, F., Márka, S., Márka, Z., Markosyan, A. S., Maros, E., Martelli, F., Martellini, L., Martin, I. W., Martin, R. M., Martynov, D. V., Marx, J. N., Mason, K., Masserot, A., Massinger, T. J., Masso-Reid, M., Matichard, F., Matone, L., Mavalvala, N., Mazumder, N., Mazzolo, G., McCarthy, R., McClelland, D. E., McCormick, S., McGuire, S. C., McIntyre, G., McIver, J., McManus, D. J., McWilliams, S. T., Meacher, D., Meadors, G. D., Meidam, J., Melatos, A., Mendell, G., Mendoza-Gandara, D., Mercer, R. A., Merilh, E., Merzougui, M., Meshkov, S., Messenger, C., Messick, C., Meyers, P. M., Mezzani, F., Miao, H., Michel, C., Middleton, H., Mikhailov, E. E., Milano, L., Miller, J., Millhouse, M., Minenkov, Y., Ming, J., Mirshekari, S., Mishra, C., Mitra, S., Mitrofanov, V. P., Mitselmakher, G., Mittleman, R., Moggi, A., Mohan, M., Mohapatra, S. R. P., Montani, M., Moore, B. C., Moore, C. J., Moraru, D., Moreno, G., Morriss, S. R., Mossavi, K., Mours, B., Mow-Lowry, C. M., Mueller, C. L., Mueller, G., Muir, A. W., Mukherjee, A., Mukherjee, D., Mukherjee, S., Mukund, N., Mullavey, A., Munch, J., Murphy, D. J., Murray, P. G., Mytidis, A., Nardecchia, I., Naticchioni, L., Nayak, R. K., Necula, V., Nedkova, K., Nelemans, G., Neri, M., Neunzert, A., Newton, G., Nguyen, T. T., Nielsen, A. B., Nissanke, S., Nitz, A., Nocera, F., Nolting, D., Normandin, M. E. N., Nuttall, L. K., Oberling, J., Ochsner, E., O'Dell, J., Oelker, E., Ogin, G. H., Oh, J. J., Oh, S. H., Ohme, F., Oliver, M., Oppermann, P., Oram, R. J., O'Reilly, B., O'Shaughnessy, R., Ott, C. D., Ottaway, D. J., Ottens, R. S., Overmier, H., Owen, B. J., Pai, A., Pai, S. A., Palamos, J. R., Palashov, O., Palomba, C., Pal-Singh, A., Pan, H., Pan, Y., Pankow, C., Pannarale, F., Pant, B. C., Paoletti, F., Paoli, A., Papa, M. A., Paris, H. R., Parker, W., Pascucci, D., Pasqualetti, A., Passaquieti, R., Passuello, D., Patricelli, B., Patrick, Z., Pearlstone, B. L., Pedraza, M., Pedurand, R., Pekowsky, L., Pele, A., Penn, S., Perreca, A., Pfeiffer, H. P., Phelps, M., Piccinni, O., Pichot, M., Pickenpack, M., Piergiovanni, F., Pierro, V., Pillant, G., Pinard, L., Pinto, I. M., Pitkin, M., Poeld, J. H., Poggiani, R., Popolizio, P., Post, A., Powell, J., Prasad, J., Predoi, V., Premachandra, S. S., Prestegard, T., Price, L. R., Prijatelj, M., Principe, M., Privitera, S., Prix, R., Prodi, G. A., Prokhorov, L., Puncken, O., Punturo, M., Puppo, P., Pürrer, M., Qi, H., Qin, J., Quetschke, V., Quintero, E. A., Quitzow-James,

R., Raab, F. J., Rabeling, D. S., Radkins, H., Raffai, P., Raja, S., Rakhmanov, M., Ramet, C. R., Rapagnani, P., Raymond, V., Razzano, M., Re, V., Read, J., Reed, C. M., Regimbau, T., Rei, L., Reid, S., Reitze, D. H., Rew, H., Reyes, S. D., Ricci, F., Riles, K., Robertson, N. A., Robie, R., Robinet, F., Rocchi, A., Rolland, L., Rollins, J. G., Roma, V. J., Romano, J. D., Romano, R., Romanov, G., Romie, J. H., Rosińska, D., Rowan, S., Rüdiger, A., Ruggi, P., Ryan, K., Sachdev, S., Sadecki, T., Sadeghian, L., Salconi, L., Saleem, M., Salemi, F., Samajdar, A., Sammut, L., Sampson, L. M., Sanchez, E. J., Sandberg, V., Sandeen, B., Sanders, G. H., Sanders, J. R., Sassolas, B., Sathyaprakash, B. S., Saulson, P. R., Sauter, O., Savage, R. L., Sawadsky, A., Schale, P., Schilling, R., Schmidt, J., Schmidt, P., Schnabel, R., Schofield, R. M. S., Schönbeck, A., Schreiber, E., Schuette, D., Schutz, B. F., Scott, J., Scott, S. M., Sellers, D., Sengupta, A. S., Sentenac, D., Sequino, V., Sergeev, A., Serna, G., Setyawati, Y., Sevigny, A., Shaddock, D. A., Shaffer, T., Shah, S., Shahriar, M. S., Shaltev, M., Shao, Z., Shapiro, B., Shawhan, P., Sheperd, A., Shoemaker, D. H., Shoemaker, D. M., Siellez, K., Siemens, X., Sigg, D., Silva, A. D., Simakov, D., Singer, A., Singer, L. P., Singh, A., Singh, R., Singhal, A., Sintes, A. M., Slagmolen, B. J. J., Smith, J. R., Smith, M. R., Smith, N. D., Smith, R. J. E., Son, E. J., Sorazu, B., Sorrentino, F., Souradeep, T., Srivastava, A. K., Staley, A., Steinke, M., Steinlechner, J., Steinlechner, S., Steinmeyer, D., Stephens, B. C., Stevenson, S. P., Stone, R., Strain, K. A., Straniero, N., Stratta, G., Strauss, N. A., Strigin, S., Sturani, R., Stuver, A. L., Summerscales, T. Z., Sun, L., Sutton, P. J., Swinkels, B. L., Szczepańczyk, M. J., Tacca, M., Talukder, D., Tanner, D. B., Tápai, M., Tarabrin, S. P., Taracchini, A., Taylor, R., Theeg, T., Thirugnanasambandam, M. P., Thomas, E. G., Thomas, M., Thomas, P., Thorne, K. A., Thorne, K. S., Thrane, E., Tiwari, S., Tiwari, V., Tokmakov, K. V., Tomlinson, C., Tonelli, M., Torres, C. V., Torrie, C. I., Töyrä, D., Travasso, F., Traylor, G., Trifirò, D., Tringali, M. C., Trozzo, L., Tse, M., Turconi, M., Tuyenbayev, D., Ugolini, D., Unnikrishnan, C. S., Urban, A. L., Usman, S. A., Vahlbruch, H., Vajente, G., Valdes, G., Vallisneri, M., van Bakel, N., van Beuzekom, M., van den Brand, J. F. J., Van Den Broeck, C., Vander-Hyde, D. C., van der Schaaf, L., van Heijningen, J. V., van Veggel, A. A., Vardaro, M., Vass, S., Vasúth, M., Vaulin, R., Vecchio,

A., Vedovato, G., Veitch, J., Veitch, P. J., Venkateswara, K., Verkindt, D., Vetrano, F., Viceré, A., Vinciguerra, S., Vine, D. J., Vinet, J.-Y., Vitale, S., Vo, T., Vocca, H., Vorvick, C., Voss, D., Vousden, W. D., Vyatchanin, S. P., Wade, A. R., Wade, L. E., Wade, M., Waldman, S. J., Walker, M., Wallace, L., Walsh, S., Wang, G., Wang, H., Wang, M., Wang, X., Wang, Y., Ward, H., Ward, R. L., Warner, J., Was, M., Weaver, B., Wei, L.-W., Weinert, M., Weinstein, A. J., Weiss, R., Welborn, T., Wen, L., Weßels, P., Westphal, T., Wette, K., Whelan, J. T., Whitcomb, S. E., White, D. J., Whiting, B. F., Wiesner, K., Wilkinson, C., Willems, P. A., Williams, L., Williams, R. D., Williamson, A. R., Willis, J. L., Willke, B., Wimmer, M. H., Winkelmann, L., Winkler, W., Wipf, C. C., Wiseman, A. G., Wittel, H., Woan, G., Worden, J., Wright, J. L., Wu, G., Yablon, J., Yakushin, I., Yam, W., Yamamoto, H., Yancey, C. C., Yap, M. J., Yu, H., Yvert, M., Zadrożny, A., Zangrando, L., Zanolin, M., Zendri, J.-P., Zevin, M., Zhang, F., Zhang, L., Zhang, M., Zhang, Y., Zhao, C., Zhou, M., Zhou, Z., Zhu, X. J., Zucker, M. E., Zuraw, S. E., and Zweizig, J. (2016). Observation of gravitational waves from a binary black hole merger. *Phys. Rev. Lett.*, 116:061102.

[2] Bakos, G., Noyes, R. W., Kovács, G., Stanek, K. Z., Sasselov, D. D., and Domsa, I. (2004). Wide-Field Millimagnitude Photometry with the HAT: A Tool for Extrasolar Planet Detection. , 116:266–277.

[3] Basri, G., Walkowicz, L. M., Batalha, N., Gilliland, R. L., Jenkins, J., Borucki, W. J., Koch, D., Caldwell, D., Dupree, A. K., Latham, D. W., Marcy, G. W., Meibom, S., and Brown, T. (2011). Photometric Variability in Kepler Target Stars. II. An Overview of Amplitude, Periodicity, and Rotation in First Quarter Data. , 141:20.

[4] Beatty, T. G. and Gaudi, B. S. (2008). Predicting the Yields of Photometric Surveys for Transiting Extrasolar Planets. , 686:1302–1330.

[5] Bertin, E. (2011). Automated Morphometry with SExtractor and PSFEx. In Evans, I. N., Accomazzi, A., Mink, D. J., and Rots, A. H., editors, *Astronomical Data Analysis Software and Systems XX*, volume 442 of *Astronomical Society of the Pacific Conference Series*, page 435.

[6] Bertin, E. and Arnouts, S. (1996). Sextractor: Software for source extraction. *Astron. Astrophys. Suppl. Ser.*, 117(2):393–404.

[7] Blackman, S. (2019). Run boy run. *The Umbrella Academy*, 1(2).

[8] Borucki, W. J., Koch, D., Basri, G., Batalha, N., Brown, T., Caldwell, D., Caldwell, J., Christensen-Dalsgaard, J., Cochran, W. D., DeVore, E., Dunham, E. W., Dupree, A. K., Gautier, T. N., Geary, J. C., Gilliland, R., Gould, A., Howell, S. B., Jenkins, J. M., Kondo, Y., Latham, D. W., Marcy, G. W., Meibom, S., Kjeldsen, H., Lissauer, J. J., Monet, D. G., Morrison, D., Sasselov, D., Tarter, J., Boss, A., Brownlee, D., Owen, T., Buzasi, D., Charbonneau, D., Doyle, L., Fortney, J., Ford, E. B., Holman, M. J., Seager, S., Steffen, J. H., Welsh, W. F., Rowe, J., Anderson, H., Buchhave, L., Ciardi, D., Walkowicz, L., Sherry, W., Horch, E., Isaacson, H., Everett, M. E., Fischer, D., Torres, G., Johnson, J. A., Endl, M., MacQueen, P., Bryson, S. T., Dotson, J., Haas, M., Kolodziejczak, J., Van Cleve, J., Chandrasekaran, H., Twicken, J. D., Quintana, E. V., Clarke, B. D., Allen, C., Li, J., Wu, H., Tenenbaum, P., Verner, E., Bruhweiler, F., Barnes, J., and Prsa, A. (2010). Kepler Planet-Detection Mission: Introduction and First Results. *Science*, 327:977.

[9] Boyajian, T. S., LaCourse, D. M., Rappaport, S. A., Fabrycky, D., Fischer, D. A., Gandolfi, D., Kennedy, G. M., Korhonen, H., Liu, M. C., Moor, A., and et al. (2016). Planet hunters ix. kic 8462852 – where's the flux? *Monthly Notices of the Royal Astronomical Society*, 457(4):3988–4004.

[10] Bozza, V., Bachelet, E., Bartolić, F., Heintz, T. M., Hoag, A. R., and Hundertmark, M. (2018). Vbbinarylensing: a public package for microlensing light-curve computation. *Monthly Notices of the Royal Astronomical Society*, 479(4):5157–5167.

[11] Brown, T. M. (2003). Expected Detection and False Alarm Rates for Transiting Jovian Planets. , 593(2):L125–L128.

[12] Bryden, G. (2020). Ukirt event detection. *The Astrophysical Journal*, XXX(YYY).

[13] Burke, C. J., Gaudi, B. S., DePoy, D. L., and Pogge, R. W. (2006). Survey for Transiting Extrasolar Planets in Stellar Systems. III. A Limit on the Fraction of Stars with Planets in the Open Cluster NGC 1245. , 132(1):210–230.

[14] Covey, K. R., Ivezić, Ž., Schlegel, D., Finkbeiner, D., Padmanabhan, N., Lupton, R. H., Agüeros, M. A., Bochanski, J. J., Hawley, S. L., West, A. A., Seth, A., Kimball, A., Gogarten, S. M., Claire, M., Haggard, D., Kaib, N., Schneider, D. P., and Sesar, B. (2007). Stellar SEDs from 0.3 to 2.5 μm: Tracing the Stellar Locus and Searching for Color Outliers in the SDSS and 2MASS. , 134:2398–2417.

[15] Cox, A. N. and Pilachowski, C. A. (2000). Allen's Astrophysical Quantities. *Physics Today*, 53(10):77.

[16] Einstein, A. (1936). Lens-like action of a star by the deviation of light in the gravitational field. *Science*, 84(2188):506–507.

[17] Gaudi, B. S. (2012). Microlensing Surveys for Exoplanets. , 50:411–453.

[18] Gehrels, N., Spergel, D., SDT, W., and Project (2015). Wide-field infrared survey telescope (wfirst) mission and synergies with lisa and ligo-virgo. *Journal of Physics: Conference Series*, 610(1):012007.

[19] Hartman, J. D. and Bakos, G. Á. (2016). VARTOOLS: A program for analyzing astronomical time-series data. *Astronomy and Computing*, 17:1–72.

[20] Ivezic, Z., Axelrod, T., Brandt, W. N., Burke, D. L., Claver, C. F., Connolly, A., Cook, K. H., Gee, P., Gilmore, D. K., Jacoby, S. H., Jones, R. L., Kahn, S. M., Kantor, J. P., Krabbendam, V. V., Lupton, R. H., Monet, D. G., Pinto, P. A., Saha, A., Schalk, T. L., Schneider, D. P., Strauss, M. A., Stubbs, C. W., Sweeney, D., Szalay, A., Thaler, J. J., Tyson, J. A., and LSST Collaboration (2008). Large Synoptic Survey Telescope: From Science Drivers To Reference Design. *Serbian Astronomical Journal*, 176:1–13.

[21] Jacklin, S., Lund, M. B., Pepper, J., and Stassun, K. G. (2015). Transiting Planets with LSST. II. Period Detection of Planets Orbiting 1 $M_{\odot}$ Hosts. , 150:34.

[22] Jacklin, S. R., Lund, M. B., Pepper, J., and Stassun, K. G. (2017). Transiting Planets with LSST. III. Detection Rate per Year of Operation. , 153(4):186.

[23] Kasting, J. F., Whitmire, D. P., and Reynolds, R. T. (1993). Habitable Zones around Main Sequence Stars. , 101:108–128.

[24] Kovács, G., Zucker, S., and Mazeh, T. (2002). A box-fitting algorithm in the search for periodic transits. , 391:369–377.

[25] LSST Science Collaboration, Abell, P., Allison, J., Anderson, S., Andrew, J., Angel, J., Armus, L., Arnett, D., Asztalos, S., Axelrod, T., and al., E. (2009). *LSST Science Book*. LSST Science Collaboration, Tucson, AZ, version 2. edition.

[26] Lund, M. B., Pepper, J., and Stassun, K. G. (2015). Transiting Planets With LSST. I. Potential for LSST Exoplanet Detection. , 149:16.

[27] Lund, M. B., Siverd, R. J., Pepper, J. A., and Stassun, K. G. (2016). Metrics for Optimization of Large Synoptic Survey Telescope Observations of Stellar Variables and Transients. , 128(2):025002.

[28] Mróz, P., Udalski, A., Skowron, J., Szymański, M. K., Soszyński, I., Wyrzykowski, Ł., Pietrukowicz, P., Kozłowski, S., Poleski, R., Ulaczyk, K., Rybicki, K., and Iwanek, P. (2019). Microlensing optical depth and event rate toward the galactic bulge from 8 yr of OGLE-IV observations. *The Astrophysical Journal Supplement Series*, 244(2):29.

[29] Nutzman, P. and Charbonneau, D. (2008). Design considerations for a ground-based transit search for habitable planets orbiting m dwarfs. *Publications of the Astronomical Society of the Pacific*, 120(865):317–327.

[30] Ochsenbein, F., Bauer, P., and Marcout, J. (2000). The VizieR database of astronomical catalogues. , 143:23–32.

[31] Paczyński, B. (1986). Gravitational microlensing by the galactic halo. , 304:1–5.

[32] Pepper, J., Kuhn, R. B., Siverd, R., James, D., and Stassun, K. (2012). The KELT-South Telescope. , 124:230–241.

[33] Pepper, J., Pogge, R. W., DePoy, D. L., Marshall, J. L., Stanek, K. Z., Stutz, A. M., Poindexter, S., Siverd, R., O'Brien, T. P., Trueblood, M., and Trueblood, P. (2007). The Kilodegree Extremely Little Telescope (KELT): A Small Robotic Telescope for Large-Area Synoptic Surveys. , 119:923–935.

[34] Poleski, R. and Yee, J. (2018). MulensModel: Microlensing light curves modeling.

[35] Pollacco, D. L., Skillen, I., Collier Cameron, A., Christian, D. J., Hellier, C., Irwin, J., Lister, T. A., Street, R. A., West, R. G., Anderson, D. R., Clarkson, W. I., Deeg, H., Enoch, B., Evans, A., Fitzsimmons, A., Haswell, C. A., Hodgkin, S., Horne, K., Kane, S. R., Keenan, F. P., Maxted, P. F. L., Norton, A. J., Osborne, J., Parley, N. R., Ryans, R. S. I., Smalley, B., Wheatley, P. J., and Wilson, D. M. (2006). The WASP Project and the SuperWASP Cameras. , 118:1407–1418.

[36] Ricker, G. R., Winn, J. N., Vanderspek, R., Latham, D. W., Bakos, G. Á., Bean, J. L., Berta-Thompson, Z. K., Brown, T. M., Buchhave, L., Butler, N. R., Butler, R. P., Chaplin, W. J., Charbonneau, D., Christensen-Dalsgaard, J., Clampin, M., Deming, D., Doty, J., De Lee, N., Dressing, C., Dunham, E. W., Endl, M., Fressin, F., Ge, J., Henning, T., Holman, M. J., Howard, A. W., Ida, S., Jenkins, J. M., Jernigan, G., Johnson, J. A., Kaltenegger, L., Kawai, N., Kjeldsen, H., Laughlin, G., Levine, A. M., Lin, D., Lissauer, J. J., MacQueen, P., Marcy, G., McCullough, P. R., Morton, T. D., Narita, N., Paegert, M., Palle, E., Pepe, F., Pepper, J., Quirrenbach, A., Rinehart, S. A., Sasselov, D., Sato, B., Seager, S., Sozzetti, A., Stassun, K. G., Sullivan, P.,

Szentgyorgyi, A., Torres, G., Udry, S., and Villasenor, J. (2015). Transiting Exoplanet Survey Satellite (TESS). *Journal of Astronomical Telescopes, Instruments, and Systems*, 1(1):014003.

[37] Ricker, G. R., Winn, J. N., Vanderspek, R., Latham, D. W., Bakos, G. , Bean, J. L., Berta-Thompson, Z. K., Brown, T. M., Buchhave, L., Butler, N. R., and et al. (2014). Transiting exoplanet survey satellite. *Journal of Astronomical Telescopes, Instruments, and Systems*, 1(1):014003.

[38] Selsis, F., Kasting, J. F., Levrard, B., Paillet, J., Ribas, I., and Delfosse, X. (2007). Habitable planets around the star Gliese 581? , 476:1373–1387.

[39] Shvartzvald, Y., Bryden, G., Gould, A., Henderson, C. B., Howell, S. B., and Beichman, C. (2017). UKIRT Microlensing Surveys as a Pathfinder for WFIRST: The Detection of Five Highly Extinguished Low-$|b|$ Events. , 153:61.

[40] Shvartzvald, Y., Calchi Novati, S., Gaudi, B. S., Bryden, G., Nataf, D. M., Penny, M. T., Beichman, C., Henderson, C. B., Jacklin, S., Schlafly, E. F., and Huston, M. J. (2018). UKIRT-2017-BLG-001Lb: A Giant Planet Detected through the Dust. , 857:L8.

[41] Skrutskie, M. F., Cutri, R. M., Stiening, R., Weinberg, M. D., Schneider, S., Carpenter, J. M., Beichman, C., Capps, R., Chester, T., Elias, J., Huchra, J., Liebert, J., Lonsdale, C., Monet, D. G., Price, S., Seitzer, P., Jarrett, T., Kirkpatrick, J. D., Gizis, J. E., Howard, E., Evans, T., Fowler, J., Fullmer, L., Hurt, R., Light, R., Kopan, E. L., Marsh, K. A., McCallon, H. L., Tam, R., Van Dyk, S., and Wheelock, S. (2006). The Two Micron All Sky Survey (2MASS). , 131(2):1163–1183.

[42] Spergel, D., Gehrels, N., Baltay, C., Bennett, D., Breckinridge, J., Donahue, M., Dressler, A., Gaudi, B. S., Greene, T., Guyon, O., Hirata, C., Kalirai, J., Kasdin, N. J., Macintosh, B., Moos, W., Perlmutter, S., Postman, M., Rauscher, B., Rhodes, J., Wang, Y., Weinberg, D., Benford, D., Hudson, M., Jeong, W. S., Mellier, Y., Traub, W., Yamada, T., Capak, P., Colbert, J., Masters, D., Penny, M., Savransky, D., Stern, D., Zimmerman, N., Barry, R., Bartusek,

L., Carpenter, K., Cheng, E., Content, D., Dekens, F., Demers, R., Grady, K., Jackson, C., Kuan, G., Kruk, J., Melton, M., Nemati, B., Parvin, B., Poberezhskiy, I., Peddie, C., Ruffa, J., Wallace, J. K., Whipple, A., Wollack, E., and Zhao, F. (2015). Wide-field infrarred survey telescope-astrophysics focused telescope assets wfirst-afta 2015 report.

[43] Stassun, K. G., Pepper, J. A., Oelkers, R., Paegert, M., De Lee, N., and Sanchis-Ojeda, R. (2014). The K2-TESS Stellar Properties Catalog. *ArXiv e-prints*.

[44] Sumi, T. and Penny, M. T. (2016). Possible Solution of the Long-standing Discrepancy in the Microlensing Optical Depth toward the Galactic Bulge by Correcting the Stellar Number Count. , 827:139.

[45] Udalski, A., Szymanski, M., Kaluzny, J., Kubiak, M., and Mateo, M. (1992). The Optical Gravitational Lensing Experiment. , 42:253–284.

[46] Vega, L. D., Stassun, K. G., Montez, R., Boyd, P. T., and Somers, G. (2017). Evidence for binarity and possible disk obscuration inKeplerObservations of the pulsating RV tau variable DF cygni. *The Astrophysical Journal*, 839(1):48.

[47] von Braun, K., Kane, S. R., and Ciardi, D. R. (2009). Observational Window Functions in Planet Transit Surveys. , 702(1):779–790.

[48] Yee, J. C., Albrow, M., Barry, R. K., Bennett, D., Bryden, G., Chung, S.-J., Gaudi, B. S., Gehrels, N., Gould, A., Penny, M. T., Rattenbury, N., Ryu, Y.-H., Skowron, J., Street, R., and Sumi, T. (2014). NASA ExoPAG Study Analysis Group 11: Preparing for the WFIRST Microlensing Survey. *ArXiv e-prints*.